CrossMark

*J. Plasma Phys.* (2022), *vol*. 88, 905880111 © The Author(s), 2022. 
Published by Cambridge University Press
doi:10.1017/S0022377822000010

# Gyrofluid analysis of electron $\beta_e$ effects on collisionless reconnection

**C. Granier** [1,2,†], **D. Borgogno** [2], **D. Grasso** [2] **and E. Tassi** [1]

[1]Université Côte d'Azur, CNRS, Observatoire de la Côte d'Azur, Laboratoire J. L. Lagrange, Boulevard de l'Observatoire, CS 34229, 06304 Nice Cedex 4, France

[2]Istituto dei Sistemi Complessi – CNR and Dipartimento di Energia, Politecnico di Torino, Torino 10129, Italy

(Received 1 October 2021; revised 29 December 2021; accepted 4 January 2022)

The linear and nonlinear evolutions of the tearing instability in a collisionless plasma with a strong guide field are analysed on the basis of a two-field Hamiltonian gyrofluid model. The model is valid for a low ion temperature and a finite $\beta_e$. The finite $\beta_e$ effect implies a magnetic perturbation along the guide field direction, and electron finite Larmor radius effects. A Hamiltonian derivation of the model is presented. A new dispersion relation of the tearing instability is derived for the case $\beta_e = 0$ and tested against numerical simulations. For $\beta_e \ll 1$ the equilibrium electron temperature is seen to enhance the linear growth rate, whereas we observe a stabilizing role when electron finite Larmor radius effects become more relevant. In the nonlinear phase, stall phases and faster than exponential phases are observed, similarly to what occurs in the presence of ion finite Larmor radius effects. Energy transfers are analysed and the conservation laws associated with the Casimir invariants of the model are also discussed. Numerical simulations seem to indicate that finite $\beta_e$ effects do not produce qualitative modifications in the structures of the Lagrangian invariants associated with Casimirs of the model.

**Key words:** astrophysical plasmas, plasma instabilities, space plasma physics

## 1. Introduction

Magnetic reconnection plays a crucial role in a broad range of plasma environments, from laboratory plasma experiments to astrophysical plasmas. It is a fundamental energy conversion process, as a result of which magnetic field energy is converted into kinetic energy and heat. In a reconnection event, the tearing instability is believed to play an important role as an onset mechanism of the process. A considerable progress in the understanding of this mechanism has been achieved through the fluid description of plasmas. The fluid framework is less costly in terms of computational resources, and physically more intuitive when compared with the kinetic framework. Fluid models, in general, are also more suitable for analytical treatment. In the non-collisional case, some reduced fluid models were designed to retain two-fluid effects (e.g. Aydemir 1992; Ottaviani & Porcelli 1993; Schep, Pegoraro & Kuvshinov 1994; Cafaro *et al.* 1998; Grasso *et al.* 1999; Del Sarto, Califano & Pegoraro 2006; Fitzpatrick & Porcelli 2007; Grasso & Tassi 2015), such as, for instance, electron inertia (Furth 1962, 1964) which is known to

† Email address for correspondence: camille.granier@oca.eu

https://doi.org/10.1017/S0022377822000010 Published online by Cambridge University Press

develop a thin current layer where modifications of the topology of the magnetic field lines can occur. These fluid models, on the other hand, neglect the effects of the electron Larmor radius, which makes it impossible to describe phenomena taking place at a microscopic scale comparable to that of the electron thermal gyroradius. Gyrofluid models are the effective tools to fill this gap. Indeed, although obtained by truncating the infinite hierarchy of equations involving the moments of the gyrokinetic equations, gyrofluid models, unlike fluid models, retain finite Larmor radius (FLR) effects and are thus valid on thermal Larmor radius scales. Also, most of the available reduced gyrofluid models, to the best of our knowledge, neglect the perturbations of the magnetic field along the direction of a guide field, the latter typically corresponding to the mean magnetic field in astrophysical plasmas (e.g. Schekochihin *et al.* 2009) or to an imposed external field in laboratory plasmas. However, even in the case of a strong guide field, such perturbations can be relevant in some nearly collisionless environments such as the solar wind, which motivates their inclusion in an analysis of collisionless reconnection. The study of reconnection for a finite $\beta_e$ can be relevant especially for plasmas with relatively large temperatures, such as in the Earth's magnetosheath, where some $\beta > 1$ values are observed, in the presence of a guide field, during reconnection events (Eastwood *et al.* 2018; Man *et al.* 2020).

In this work, we make use of a gyrofluid model to study the linear and nonlinear evolution of the tearing instability in a collisionless plasma with strong guide field. This study is based on a two-field gyrofluid model that has been derived from gyrokinetic equations in Tassi, Passot & Sulem (2020), assuming a quasistatic closure. With respect to the above-mentioned reduced fluid models, such a gyrofluid model accounts for both finite electron Larmor radius effects and perturbations parallel to the direction of the guide field. The model is taken within the asymptotic cold-ion limit, although we present a small set of simulations performed in the limit of hot ions to reflect the differences and possible consequences of this limit. A more in-depth study of the hot-ion limit could be done in a subsequent work. Our gyrofluid model is valid for finite $\beta_e$ values, where $\beta_e$ is the ratio between the electron pressure and the magnetic pressure based on the guide field. We remark that finite $\beta_e$ effects were also taken into account in the model by Fitzpatrick & Porcelli (2004, 2007). However, in that model, electron FLR effects were neglected.

We consider magnetic reconnection taking place in a two dimensional (2-D) plane, perpendicular to the guide field. Reconnection is mediated by electron inertia and by electron FLR, which makes the process non-dissipative, unlike reconnection driven by electrical collisional resistivity. As with many dissipationless fluid and gyrofluid models, the gyrofluid model under consideration also possesses a Hamiltonian structure, which reveals the presence of two Lagrangian invariants and gives the expression of the conserved total energy of the system. With this we can obtain further information about how $\beta_e$ can influence the distribution of the different components of the total energy.

In the limit $\beta_e \to 0$ (in the following also referred to as the 'fluid' limit), the model corresponds to the two-field fluid model of Schep *et al.* (1994). This fluid model has long been used to study the tearing instability, and a relevant dispersion relation for the collisionless tearing mode, applicable to this model, has been derived in Porcelli (1991) and is valid for any value of $\Delta'$. We present in this article a new analytical formula, whose derivation is presented in Appendix A and follows the procedure used by Grasso, Ottaviani & Porcelli (2002), which is carried out in real space and resorts to the constant-$\psi$ approximation (Furth, Killeen & Rosenbluth 1963). This new formula differs from the small tearing parameter $\Delta'$ limit of the formula of Porcelli (1991), by the presence of a small corrective term. These two formulae are tested against numerical simulations and, in its regime of validity, our new relation shows a better agreement with the numerical growth rate.

https://doi.org/10.1017/S0022377822000010 Published online by Cambridge University Press

We studied numerically the effect of a finite $\beta_e$ in the linear and nonlinear phase of the tearing instability. For the linear phase, we first isolate the effect of varying $\beta_e$ by keeping fixed all the other parameters of the system. In this setting we observe a stabilizing role of the $\beta_e$ parameter. The stabilizing effect is then seen to be reduced when increasing the normalized electron skin depth $d_e$. A partial justification of this behaviour can be given analytically considering the small FLR limit of the model. We remark that varying $\beta_e$ with fixed $d_e$ and $\rho_s$ amounts to varying the normalized thermal electron Larmor radius $\rho_e$ at fixed $\rho_s$. Subsequently, we consider the effect of varying $\beta_e$ while keeping a fixed mass ratio. The previously mentioned stabilizing role of $\beta_e$ is then concomitant with the destabilizing role of the normalized sonic Larmor radius $\rho_s$. The growth rate is thus evaluated for different values of the parameters $d_e$, $\rho_s$ and $\rho_e$. These parameters are associated with different physical scales and are absent in the usual reduced magnetohydrodynamics description. The stabilizing effect of the tearing mode when increasing $\beta_e$ and $m_e/m_i$ is in agreement with Numata *et al.* (2011). We also obtained the same scaling as the one of Numata & Loureiro (2015) when varying $\beta_e$ and $d_e$. Both these studies were performed with a gyrokinetic model and we refer to the scaling they obtained within the non-/semicollisional limit. In the nonlinear phase, we find the explosive growth rate (Aydemir 1992; Ottaviani & Porcelli 1993) which has been obtained as well in the gyrofluid study of Biancalani & Scott (2012) that was considering low $\beta_e$ and ion FLR, but no electron FLR effects. We investigate how the effects of $\beta_e$ affects this faster than exponential growth.

The reconnection process described by Hamiltonian reduced fluid and gyrofluid models has been analysed in terms of Lagrangian invariants in several cases in the past (Cafaro *et al.* 1998; Grasso *et al.* 2001; Grasso, Tassi & Waelbroeck 2010; Comisso *et al.* 2013; Grasso & Tassi 2015). The effect of both electron FLR effects and parallel magnetic perturbations on the structure of such invariants has not been studied so far, though. In this paper we present the behaviour of the two topological invariants of the system. They extend the Lagrangian invariants of simpler models that do not account for $\beta_e$ effects and behave similarly.

The paper is organized as follows. In § 2 we derive the gyrofluid model adopted for the analysis. The procedure we follow for the derivation automatically provides the Hamiltonian structure of the model. Section 3 contains a review of the linear theory and a new dispersion relation for the case $\beta_e = 0$. We also present the results of numerical simulations in the linear phase, for finite $\beta_e$. In § 4 the results obtained in the nonlinear phase are presented and the gyrofluid version is compared with the fluid version. In this section we also study the impact of a finite $\beta_e$ on the evolution of the different energy components. Section 5 presents the conservation laws and the evolution of the Lagrangian invariants of the model. In Appendix A we present the derivation of the new dispersion relation, which is based on the asymptotic matching theory.

## 2. The gyrofluid model

We begin by considering the model given by the evolution equations

$$\frac{\partial N_i}{\partial t} + [G_{10i}\phi + \tau_{\perp_i}\rho_{s_\perp}^2 2G_{20i}B_\parallel, N_i] - [G_{10i}A_\parallel, U_i] = 0, \tag{2.1}$$

$$\frac{\partial}{\partial t}(U_i + G_{10i}A_\parallel) + [G_{10i}\phi + \tau_{\perp_i}\rho_{s_\perp}^2 2G_{20i}B_\parallel, U_i + G_{10i}A_\parallel] - \frac{\tau_{\perp_i}\rho_{s_\perp}^2}{\Theta_i}[G_{10i}A_\parallel, N_i] = 0, \tag{2.2}$$

https://doi.org/10.1017/S0022377822000010 Published online by Cambridge University Press

$$\frac{\partial N_e}{\partial t} + [G_{10e}\phi - \rho_{s_\perp}^2 2G_{20e}B_\parallel, N_e] - [G_{10e}A_\parallel, U_e] = 0, \tag{2.3}$$

$$\frac{\partial}{\partial t}(G_{10e}A_\parallel - d_e^2 U_e) + [G_{10e}\phi - \rho_{s_\perp}^2 2G_{20e}B_\parallel, G_{10e}A_\parallel - d_e^2 U_e] + \frac{\rho_{s_\perp}^2}{\Theta_e}[G_{10e}A_\parallel, N_e] = 0, \tag{2.4}$$

complemented by the static relations

$$\begin{aligned} &G_{10i}N_i - G_{10e}N_e + (1-\Theta_i)\Gamma_{0i}\frac{\phi}{\tau_{\perp_i}\rho_{s_\perp}^2} + (1-\Theta_e)\Gamma_{0e}\frac{\phi}{\rho_{s_\perp}^2} + (\Theta_i G_{10i}^2 - 1)\frac{\phi}{\tau_{\perp_i}\rho_{s_\perp}^2} \\ &\quad + (\Theta_e G_{10e}^2 - 1)\frac{\phi}{\rho_{s_\perp}^2} + (\Theta_i G_{10i}2G_{20i} - \Theta_e G_{10e}2G_{20e})B_\parallel \\ &\quad + ((1-\Theta_i)(\Gamma_{0i} - \Gamma_{1i}) - (1-\Theta_e)(\Gamma_{0e} - \Gamma_{1e}))B_\parallel = 0, \end{aligned} \tag{2.5}$$

$$\begin{aligned} \nabla_\perp^2 A_\parallel = &\left(\left(1 - \frac{1}{\Theta_e}\right)(1-\Gamma_{0e})\frac{1}{d_e^2} + \left(1 - \frac{1}{\Theta_i}\right)(1-\Gamma_{0i})\frac{1}{d_i^2}\right)A_\parallel \\ &+ G_{10e}U_e - G_{10i}U_i, \end{aligned} \tag{2.6}$$

$$\begin{aligned} B_\parallel = -\frac{\beta_{\perp_e}}{2}\Bigg(&\tau_{\perp_i}2G_{20i}N_i + 2G_{20e}N_e + (1-\Theta_i)(\Gamma_{0i} - \Gamma_{1i})\frac{\phi}{\rho_{s_\perp}^2} \\ &- (1-\Theta_e)(\Gamma_{0e} - \Gamma_{1e})\frac{\phi}{\rho_{s_\perp}^2} + \Theta_i G_{10i}2G_{20i}\frac{\phi}{\rho_{s_\perp}^2} - \Theta_e G_{10e}2G_{20e}\frac{\phi}{\rho_{s_\perp}^2} + \Theta_i\tau_{\perp_i}4G_{20i}^2 B_\parallel \\ &+ \Theta_e 4G_{20e}^2 B_\parallel + \tau_{\perp_i}2(1-\Theta_i)(\Gamma_{0i} - \Gamma_{1i})B_\parallel + 2(1-\Theta_e)(\Gamma_{0e} - \Gamma_{1e})B_\parallel\Bigg). \end{aligned} \tag{2.7}$$

Equations (2.1) and (2.3) correspond to the ion and electron gyrocentre continuity equations, respectively, whereas (2.2) and (2.4) refer to the ion and electron momentum conservation laws, along the guide field direction.

The static relations (2.5), (2.6) and (2.7) descend from quasineutrality and from the projections of Ampère's law along directions parallel and perpendicular to the guide field, respectively.

The system (2.1)–(2.7), although written with a different normalization, constitutes the Hamiltonian four-field model derived by Tassi *et al.* (2020), taken in the 2-D limit (assuming that all the independent variables do not vary along the direction of the guide field).

The model is formulated in a slab geometry adopting a Cartesian coordinate system $(x, y, z)$. We indicate with $N_s$ and $U_s$ the fluctuations of the gyrocentre densities and velocities parallel to the guide field, respectively, for the species $s$, with $s = e$ for electrons and $s = i$ for ions. The symbols $A_\parallel, B_\parallel$ and $\phi$, on the other hand, correspond to the fluctuations of the $z$ component of the magnetic vector potential, to the parallel magnetic perturbations and to the fluctuations of the electrostatic potential, respectively. The fields $N_{e,i}, U_{e,i}, A_\parallel, B_\parallel$ and $\phi$ depend on the time variable $t$ and on the spatial coordinates $x$ and $y$, which belong to the domain $\mathcal{D} = \{-L_x \leq x \leq L_x, -L_y \leq y \leq L_y\}$, with $L_x$ and $L_y$ being positive constants. Periodic boundary conditions are imposed on the domain $\mathcal{D}$. The operator $[\,,\,]$ is the canonical Poisson bracket and is defined by $[f, g] = \partial_x f \partial_y g - \partial_y f \partial_x g$, for two functions $f$ and $g$.

https://doi.org/10.1017/S0022377822000010 Published online by Cambridge University Press

We write the normalized magnetic field in the form

$$\boldsymbol{B}(x, y, z, t) \approx \hat{z} + \frac{\hat{d}_i}{L} B_{\parallel}(x, y, z, t)\hat{z} + \nabla A_{\parallel}(x, y, z, t) \times \hat{z}, \tag{2.8}$$

with $\hat{z}$ indicating the unit vector along the $z$ direction, with $L$ a characteristic equilibrium scale length and with $\hat{d}_i = c\sqrt{m_i/(4\pi e^2 n_0)}$ the ion skin depth. We denote by $m_i$ the ion mass, by $e$ the proton charge, by $c$ the speed of light and $n_0$ the equilibrium density (equal for ions and electrons). The first term on the right-hand side of (2.8) accounts for the strong guide field. In (2.8) only up to the first order terms in the fluctuations are shown, and the higher-order contributions, which guarantee $\nabla \cdot \boldsymbol{B} = 0$, are neglected. The normalization of the variables used in (2.1)–(2.7) is the following:

$$t = \frac{v_A}{L}\hat{t}, \quad x = \frac{\hat{x}}{L}, \quad y = \frac{\hat{y}}{L}, \tag{2.9a–c}$$

$$N_{e,i} = \frac{L}{\hat{d}_i}\frac{\hat{N}_{e,i}}{n_0}, \quad U_{e,i} = \frac{L}{\hat{d}_i}\frac{\hat{U}_{e,i}}{v_A}, \tag{2.10a,b}$$

$$A_{\parallel} = \frac{\hat{A}_{\parallel}}{LB_0}, \quad B_{\parallel} = \frac{L}{\hat{d}_i}\frac{\hat{B}_{\parallel}}{B_0}, \quad \phi = \frac{c}{v_A}\frac{\hat{\phi}}{LB_0}, \tag{2.11a–c}$$

where the hat indicates dimensional quantities, $B_0$ is the amplitude of the guide field and $v_A = B_0/\sqrt{4\pi m_i n_0}$ is the Alfvén speed.

Independent parameters in the model are $\beta_{\perp_e}$, $\tau_{\perp_i}$, $\rho_{s_\perp}$, $\Theta_e$, $\Theta_i$ and $d_e$, corresponding to the ratio between equilibrium electron pressure and magnetic guide field pressure, to the ratio between equilibrium perpendicular ion and electron temperatures, to the normalized sonic Larmor radius, to the ratio between the equilibrium perpendicular and parallel temperature for electrons and ions, and to the normalized perpendicular electron skin depth, respectively. These parameters are defined as

$$\beta_{\perp_e} = 8\pi\frac{n_0 T_{0_{\perp e}}}{B_0^2}, \quad \tau_{\perp_i} = \frac{T_{0_{\perp i}}}{T_{0_{\perp e}}}, \quad \rho_{s_\perp} = \frac{1}{L}\sqrt{\frac{T_{0_{\perp e}}}{m_i}}\frac{m_i c}{eB_0}, \tag{2.12a–c}$$

$$\Theta_e = \frac{T_{0_{\perp e}}}{T_{0_{\parallel e}}}, \quad \Theta_i = \frac{T_{0_{\perp i}}}{T_{0_{\parallel i}}}, \quad d_e = \frac{1}{L}c\sqrt{\frac{m_e}{4\pi e^2 n_0}}, \tag{2.13a–c}$$

where $T_{0_{\perp s}}$ and $T_{0_{\parallel s}}$ are the perpendicular and parallel equilibrium temperatures for the species $s$, respectively, and $m_e$ is the electron mass. Note that $\rho_{s_\perp}/\sqrt{\beta_{\perp_e}/2} = d_i$, where $d_i = \hat{d}_i/L$ is the normalized ion skin depth.

Electron and ion gyroaverage operators are associated with corresponding Fourier multipliers in the following way:

$$G_{10e} = 2G_{20e} \to \exp\left(-k_\perp^2\frac{\beta_{\perp_e}}{4}d_e^2\right), \tag{2.14}$$

$$G_{10i} = 2G_{20i} \to \exp\left(-k_\perp^2\frac{\tau_{\perp_i}}{2}\rho_{s_\perp}^2\right) \tag{2.15}$$

https://doi.org/10.1017/S0022377822000010 Published online by Cambridge University Press

and

$$\Gamma_{0e} \to \mathrm{I}_0\left(k_\perp^2 \frac{\beta_{\perp_e}}{2} d_e^2\right) \exp\left(-k_\perp^2 \frac{\beta_{\perp_e}}{2} d_e^2\right), \quad \Gamma_{1e} \to \mathrm{I}_1\left(k_\perp^2 \frac{\beta_{\perp_e}}{2} d_e^2\right) \exp\left(-k_\perp^2 \frac{\beta_{\perp_e}}{2} d_e^2\right), \tag{2.16a,b}$$

$$\Gamma_{0i} \to \mathrm{I}_0\left(k_\perp^2 \tau_{\perp_i} \rho_{s_\perp}^2\right) \exp(-k_\perp^2 \tau_{\perp_i} \rho_{s_\perp}^2), \quad \Gamma_{1i} \to \mathrm{I}_1\left(k_\perp^2 \tau_{\perp_i} \rho_{s_\perp}^2\right) \exp(-k_\perp^2 \tau_{\perp_i} \rho_{s_\perp}^2), \tag{2.17a,b}$$

where $\mathrm{I}_n$ are the modified Bessel functions of order $n$ and $k_\perp^2 = \sqrt{k_x^2 + k_y^2}$ is the perpendicular wavenumber.

For the range of parameters adopted in our analysis, the gyroaverage operators $G_{10e}$ and $G_{10i}$, corresponding to those introduced by Brizard (1992), are shown to be adequate. Nevertheless, different gyroaverage operators, described in the papers Dorland & Hammett (1993) and Mandell, Dorland & Landreman (2018), have proved to provide in very good agreement with the linear kinetic theory for a wider range of scales and are widespread in gyrofluid numerical codes.

We define the dynamical variables

$$A_i = G_{10i} A_\parallel + d_i^2 U_i, \quad A_e = G_{10e} A_\parallel - d_e^2 U_e. \tag{2.18a,b}$$

The fields $A_i$ and $A_e$ are proportional to the parallel canonical fluid momenta, based on gyroaveraged magnetic potentials.

The two static relations (2.5) and (2.7) can be seen, in Fourier space, as an inhomogeneous linear system with the Fourier coefficients of $\phi$ and $B_\parallel$ as unknowns, for given $N_{i,e}$. From the solution of this system, one can express the fields $\phi$ and $B_\parallel$ in terms of $N_i$ and $N_e$, by means of relations of the form

$$B_\parallel = \mathcal{L}_B(N_i, N_e), \quad \phi = \mathcal{L}_\phi(N_i, N_e), \tag{2.19a,b}$$

where $\mathcal{L}_B$ and $\mathcal{L}_\phi$ are operators, the explicit form of which can easily be provided in Fourier space. Similarly, using the relations (2.6) and (2.18a,b), one can express $U_e$ and $U_i$ in the form

$$U_e = \mathcal{L}_{U_e}(A_i, A_e), \quad U_i = \mathcal{L}_{U_i}(A_i, A_e), \tag{2.20a,b}$$

where $\mathcal{L}_{U_e}$ and $\mathcal{L}_{U_i}$ are also operators, the explicit expression of which can be given in Fourier space.

The model (2.1)–(2.7) can be formulated as an infinite-dimensional Hamiltonian system, adopting the four fields $N_i$, $N_e$, $A_i$ and $A_e$ as dynamical variables (Tassi *et al.* 2020).

The corresponding Hamiltonian structure consists of the Hamiltonian functional

$$\begin{aligned} H(N_i, N_e, A_i, A_e) = \frac{1}{2} \int \mathrm{d}^2x \Bigg( & \frac{\tau_{\perp_i} \rho_{s_\perp}^2}{\Theta_i} N_i^2 + \frac{\rho_{s_\perp}^2}{\Theta_e} N_e^2 + A_i \mathcal{L}_{U_i}(A_i, A_e) \\ & - A_e \mathcal{L}_{U_e}(A_i, A_e) + N_i(G_{10i} \mathcal{L}_\phi(N_i, N_e) + \tau_{\perp_i} \rho_{s_\perp}^2 2 G_{20i} \mathcal{L}_B(N_i, N_e)) \\ & - N_e(G_{10e} \mathcal{L}_\phi(N_i, N_e) - \rho_{s_\perp}^2 2 G_{20e} \mathcal{L}_B(N_i, N_e)) \Bigg) \end{aligned} \tag{2.21}$$

https://doi.org/10.1017/S0022377822000010 Published online by Cambridge University Press

and of the Poisson bracket

$$\{F, G\} = -\int \mathrm{d}^2x \left( N_i \left( [F_{N_i}, G_{N_i}] + \tau_{\perp_i} \frac{2}{\beta_{\perp_e}} \frac{\rho_{s_\perp}^4}{\Theta_i} [F_{A_i}, G_{A_i}] \right) \right.$$
$$+ A_i \left( [F_{A_i}, G_{N_i}] + [F_{N_i}, G_{A_i}] \right) - N_e \left( [F_{N_e}, G_{N_e}] + d_e^2 \frac{\rho_{s_\perp}^2}{\Theta_e} [F_{A_e}, G_{A_e}] \right)$$
$$\left. - A_e ([F_{A_e}, G_{N_e}] + [F_{N_e}, G_{A_e}]) \right), \tag{2.22}$$

where subscripts on functionals indicate functional derivatives, so that, for instance, $F_{N_i} = \delta F / \delta N_i$. Using the Hamiltonian (2.21) and the Poisson bracket (2.22), the four equations (2.1)–(2.4) can be obtained from the Hamiltonian form (Morrison 1998)

$$\frac{\partial \chi}{\partial t} = \{\chi, H\}, \tag{2.23}$$

replacing $\chi$ with $N_i$, $N_e$, $A_i$ and $A_e$. This Hamiltonian four-field gyrofluid model, although greatly simplified with respect to the original gyrokinetic system, is still amenable to a further reduction, concerning in particular the ion dynamics which, for the analysis of reconnection of interest here, was shown not to be crucially relevant (Numata *et al.* 2011; Comisso *et al.* 2013). Also, we carry out most of the analysis in the isotropic cold-ion limit, a simplifying assumption which is also helpful for comparison with previous works. Nevertheless, some comments will be also provided with regard to the opposite limit of equilibrium ion temperature much larger than the electron one. On the other hand, in carrying out the reduction procedure, we find it important to preserve a Hamiltonian structure, which avoids the introduction of uncontrolled dissipation in the system and also allows for a more direct comparison with previous Hamiltonian models for reconnection, in particular with the two-field model considered by Cafaro *et al.* (1998), Grasso *et al.* (2001), Del Sarto *et al.* (2006) and Del Sarto, Califano & Pegoraro (2003). In particular, we intend to obtain a Hamiltonian reduced version of the four-field model (2.1)–(2.7), in which the gyrocentre ion density fluctuations $N_i$ and ion gyrocentre parallel velocity fluctuations $U_i$ are neglected, the ion equilibrium temperature is isotropic, and ions are taken to be cold. The latter four conditions amount to impose

$$N_i = 0, \quad U_i = 0, \quad \Theta_i = 1 \tag{2.24a–c}$$

and take the limit

$$\tau_{\perp_i} \to 0. \tag{2.25}$$

Further insight about the assumptions $N_i = U_i = 0$ can be obtained expressing these assumptions in terms of particle moments, instead of gyrocentre moments. We can write the assumption $N_i = 0$ in terms of the normalized particle density fluctuation $n_i$ as

$$n_i = N_i + \nabla_\perp^2 \phi + B_\parallel, \tag{2.26}$$

valid in the limit $\tau_{\perp_i} \to 0$ and $\Theta_i = 1$ (Brizard 1992). Neglecting $N_i$ in (2.26) thus amounts to assuming that the ion density response is due only to the ion polarization (second term on the right-hand side of (2.26)) and to the parallel magnetic perturbation $B_\parallel$. In the low-$\beta$ limit, the influence of $B_\parallel$ becomes negligible and (2.26) corresponds to a solution for

https://doi.org/10.1017/S0022377822000010 Published online by Cambridge University Press

the ion response derived by the kinetic theory of Schep *et al.* (1994). With regard to the assumption that neglects the evolution of the ion gyrocentre parallel velocity, $U_i = 0$, the relation with the normalized parallel ion velocity $u_i$ is simply given by $U_i = u_i = 0$ and ions are assumed to be immobile along the guide field direction, which is reasonable by virtue of the larger ion inertia. Such assumptions can also be justified by the fact that the evolution of ion gyrocentre density and parallel velocity, at least when their initial conditions are $N_i = U_i = 0$, have been shown to have a negligible role in simulations of reconnection in Comisso *et al.* (2012).

Because we want to perform this reduction while preserving a Hamiltonian structure, we apply the conditions (2.24*a–c*) and (2.25) at the level of the Hamiltonian structure, instead of applying them directly to the equations of motion. The latter procedure would indeed produce no information about the Hamiltonian structure of the resulting model.

As a first step, we impose the conditions (2.24*a–c*)–(2.25) in the static relations (2.5)–(2.7), which leads to

$$\left(\frac{(1-\Theta_e)}{\rho_{s_\perp}^2}\Gamma_{0e} + \frac{(\Theta_e G_{10e}^2 - 1)}{\rho_{s_\perp}^2} + \nabla_\perp^2\right)\phi - (\Theta_e G_{10e} 2G_{20e} - 1 + (1-\Theta_e)(\Gamma_{0e} - \Gamma_{1e}))\, B_\parallel = G_{10e} N_e, \tag{2.27}$$

$$\left(\left(1 - \frac{1}{\Theta_e}\right)\frac{(\Gamma_{0e}-1)}{d_e^2} + \nabla_\perp^2\right) A_\parallel = G_{10e} U_e, \tag{2.28}$$

$$(\Theta_e G_{10e} 2G_{20e} + (1-\Theta_e)(\Gamma_{0e} - \Gamma_{1e}) - 1)\,\frac{\phi}{\rho_{s_\perp}^2} - \left(\frac{2}{\beta_{\perp_e}} + 2(1-\Theta_e)(\Gamma_{0e} - \Gamma_{1e}) + 4\Theta_e G_{20e}^2\right) B_\parallel = 2G_{20e} N_e. \tag{2.29}$$

The three relations (2.27)–(2.29), together with the definition of $A_e$ in (2.18*a*,*b*), make it possible to express $B_\parallel$, $\phi$ and $U_e$, in terms of the two dynamical variables $N_e$ and $A_e$, according to

$$B_\parallel = \mathcal{L}_{B0} N_e, \quad \phi = \mathcal{L}_{\phi 0} N_e, \quad U_e = \mathcal{L}_{U_e 0} A_e, \tag{2.30$a$–$c$}$$

where $\mathcal{L}_{B0}$, $\mathcal{L}_{\phi 0}$ and $\mathcal{L}_{U_e 0}$ are symmetric operators, i.e. operators $\mathcal{L}$ such that $\int \mathrm{d}^2x\, f \mathcal{L} g = \int \mathrm{d}^2x\, g \mathcal{L} f$, for two functions $f$ and $g$. As next step, we impose the conditions (2.24*a–c*)–(2.25) on the Hamiltonian (2.21), which reduces the Hamiltonian to the following functional of the only two dynamical variables $N_e$ and $A_e$:

$$H(N_e, A_e) = \frac{1}{2}\int \mathrm{d}^2x \left(\frac{\rho_{s_\perp}^2}{\Theta_e} N_e^2 - A_e \mathcal{L}_{U_e 0} A_e - N_e (G_{10e} \mathcal{L}_{\phi 0} N_e - \rho_{s_\perp}^2 2G_{20e} \mathcal{L}_{B0} N_e)\right). \tag{2.31}$$

With regard to the Poisson bracket (2.22), we can consider its limit as $\tau_{\perp_i} \to 0$, given that the bilinear form (2.22) is a valid Poisson bracket for any value of $\tau_{\perp_i}$. On the other hand, in general, we cannot impose directly the conditions (2.24*a–c*) in the bracket, as this operation does not guarantee that the resulting bilinear form satisfies the Jacobi identity. However, we remark that the set of functionals of the two dynamical variables $N_e$ and $A_e$, which the reduced Hamiltonian (2.31) belongs to, forms a subalgebra of the algebra of functionals of $N_i$, $N_e$, $A_i$ and $A_e$, with respect to the Poisson bracket (2.22). Indeed, if $F$ and $G$ are two functionals of $N_e$ and $A_e$ only, $\{F, G\}$ is again a functional of $N_e$ and $A_e$

https://doi.org/10.1017/S0022377822000010 Published online by Cambridge University Press

only. One can in particular restrict to the part of the bracket (2.22) involving functional derivatives only with respect to $N_e$ and $A_e$, the other terms yielding vanishing contributions when evaluated on functionals of $N_e$ and $A_e$ only. The resulting Poisson bracket therefore reads

$$\{F, G\} = \int \mathrm{d}^2x \left( N_e([F_{N_e}, G_{N_e}] + d_e^2 \frac{\rho_{s_\perp}^2}{\Theta_e}[F_{A_e}, G_{A_e}]) + A_e([F_{A_e}, G_{N_e}] + [F_{N_e}, G_{A_e}]) \right). \tag{2.32}$$

We remark that the Poisson bracket (2.32) has the same form as that of the model investigated by Cafaro *et al.* (1998) and by Grasso *et al.* (2001).

The resulting reduced two-field model, accounting for the conditions (2.24*a–c*)–(2.25), can then be obtained from the Hamiltonian (2.31) and the Poisson bracket (2.32). The corresponding evolution equations read

$$\frac{\partial N_e}{\partial t} + [G_{10e}\phi - \rho_{s_\perp}^2 2G_{20e}B_\parallel, N_e] - [G_{10e}A_\parallel, U_e] = 0, \tag{2.33}$$

$$\frac{\partial A_e}{\partial t} + [G_{10e}\phi - \rho_{s_\perp}^2 2G_{20e}B_\parallel, A_e] + \frac{\rho_{s_\perp}^2}{\Theta_e}[G_{10e}A_\parallel, N_e] = 0, \tag{2.34}$$

where $B_\parallel$, $\phi$ and $U_e$ are related to $N_e$ and $A_e$ by means of (2.18*a*,*b*) and (2.27)–(2.29).

We now impose electron temperature isotropy (i.e. setting $T_{0\perp e} = T_{0\parallel e} = T_{0e}$, corresponding to $\Theta_e = 1$) and the evolution equations are reduced to

$$\frac{\partial N_e}{\partial t} + [G_{10e}\phi - \rho_s^2 2G_{20e}B_\parallel, N_e] - [G_{10e}A_\parallel, U_e] = 0, \tag{2.35}$$

$$\frac{\partial A_e}{\partial t} + [G_{10e}\phi - \rho_s^2 2G_{20e}B_\parallel, A_e] + \rho_s^2[G_{10e}A_\parallel, N_e] = 0, \tag{2.36}$$

complemented by the equations

$$\left(\frac{G_{10e}^2 - 1}{\rho_s^2} + \nabla_\perp^2\right)\phi - (G_{10e}2G_{20e} - 1)\, B_\parallel = G_{10e}N_e, \tag{2.37}$$

$$\nabla_\perp^2 A_\parallel = G_{10e}U_e, \tag{2.38}$$

$$(G_{10e}2G_{20e} - 1)\frac{\phi}{\rho_s^2} - \left(\frac{2}{\beta_e} + 4G_{20e}^2\right)B_\parallel = 2G_{20e}N_e. \tag{2.39}$$

Equations (2.35), (2.36) and (2.37)–(2.39) correspond to the gyrofluid model adopted for the subsequent analysis of magnetic reconnection.

## 3. Linear phase

### 3.1. *Linear theory for $\beta_e \to 0$*

In this subsection we focus on the regime for which the electron FLR effects and the parallel magnetic perturbations are negligible. The limit of vanishing thermal electron Larmor radius, i.e. $\rho_e = d_e\sqrt{\beta_e/2} \to 0$, is adopted by considering $\beta_e \to 0$ and $m_e/m_i \to 0$. This limit enables us to reduce the gyrofluid model (2.35)–(2.39) to the fluid model of Schep *et al.* (1994) and Cafaro *et al.* (1998), for which the tearing instability has been extensively studied in the past (Porcelli 1991; Grasso *et al.* 1999, 2001).

https://doi.org/10.1017/S0022377822000010 Published online by Cambridge University Press

When assuming $\beta_e \to 0$ for a fixed $d_e$, the gyroaverage operators can be approximated in the Fourier space in the following way:

$$\left.\begin{aligned} G_{10e}f(x,y) &= \left(1+\rho_e^2\nabla_\perp^2\right)f(x,y)+O(\rho_e^4),\\ G_{20e}f(x,y) &= \tfrac{1}{2}\left(1+\rho_e^2\nabla_\perp^2\right)f(x,y)+O(\rho_e^4). \end{aligned}\right\} \tag{3.1}$$

Using this development in (2.35)–(2.39) and neglecting the first-order correction, we obtain the evolution equations (Schep *et al.* 1994)

$$\frac{\partial \nabla_\perp^2\phi}{\partial t}+[\phi,\nabla_\perp^2\phi]-[A_\parallel,\nabla_\perp^2 A_\parallel]=0, \tag{3.2}$$

$$\frac{\partial}{\partial t}\left(A_\parallel-d_e^2\nabla_\perp^2 A_\parallel\right)+\left[\phi,A_\parallel-d_e^2\nabla_\perp^2 A_\parallel\right]-\rho_s^2[\nabla_\perp^2\phi,A_\parallel]=0. \tag{3.3}$$

We assume an equilibrium given by

$$\phi^{(0)}(x)=0,\quad A_\parallel^{(0)}(x)=\frac{\lambda}{\cosh^2\left(\dfrac{x}{\lambda}\right)}, \tag{3.4a,b}$$

where $\lambda$ is a parameter that stretches the equilibrium scale length and modifies the equilibrium amplitude. We consider the perturbations

$$\begin{aligned} A_\parallel^{(1)}(x,y,t) &= \tilde{A}(x)\exp(\gamma t+\mathrm{i}k_y y)+\bar{\tilde{A}}(x)\exp(\gamma t-\mathrm{i}k_y y),\\ \phi^{(1)}(x,y,t) &= \tilde{\phi}(x)\exp(\gamma t+\mathrm{i}k_y y)+\bar{\tilde{\phi}}(x)\exp(\gamma t-\mathrm{i}k_y y), \end{aligned} \tag{3.5a,b}$$

where $\gamma$ is the growth rate of the instability, $k_y=\pi m/L_y$ is the wavenumber, with $m\in\mathbb{N}$, and the overbar refers to the complex conjugate. We look for even solutions for $\tilde{A}(x)$ and odd solutions for $\tilde{\phi}(x)$ as in the standard tearing problem for purely growing, marginally stable or decaying perturbations. This is guaranteed if $\gamma$ is a real quantity. Therefore, we discard solutions yielding $\gamma$ with an imaginary part. The collisionless tearing mode has been studied in Porcelli (1991) for the $m=1$ mode in toroidal geometry and the results can be adapted to the model (3.2)–(3.3). In particular, a dispersion relation has been obtained analytically and is valid for small and large values of the tearing stability parameter $\Delta'$, with

$$\Delta'=\lim_{x\to 0^+}\frac{\tilde{A}'_{\mathrm{out}}}{\tilde{A}_{\mathrm{out}}}-\lim_{x\to 0^-}\frac{\tilde{A}'_{\mathrm{out}}}{\tilde{A}_{\mathrm{out}}}, \tag{3.6}$$

where $\tilde{A}_{\mathrm{out}}$ is the solution for $\tilde{A}$ of the linearized system in the outer region (see also Appendix A). The tearing index, $\Delta'$, is a common measure of the discontinuity of the logarithmic derivative of $\tilde{A}_{\mathrm{out}}$ at the resonant surface. The dispersion relation is given by (Porcelli 1991; Fitzpatrick 2010)

$$\frac{\pi}{2}\left(\frac{\lambda\gamma}{2k_y}\right)^2=-\rho_s\frac{\pi}{\Delta'}+\rho_s^2 d_e\frac{2k_y}{\gamma\lambda}. \tag{3.7}$$

In the limit $d_e^{2/3}\rho_s^{1/3}\Delta'\ll 1$, the relation (3.7) is reduced to

$$\gamma=2k_y\frac{d_e\rho_s}{\pi\lambda}\Delta'. \tag{3.8}$$

In Appendix A of this paper, we present the derivation of a new dispersion relation valid in the limit $\Delta'\gamma d_e/(k_y\rho_s)\ll 1$. In the appropriate regime of validity, the new dispersion

https://doi.org/10.1017/S0022377822000010 Published online by Cambridge University Press

| No. | Assumptions used | |
|---|---|---|
| 1 | Time variation of the perturbation is slow | $\dfrac{\gamma}{k_y} \ll 1$ |
| 2 | Smallness of the inner scales | $\dfrac{\gamma d_e}{k_y \rho_s} \ll \rho_s \ll 1$ |
| 3 | Use of the constant $\psi$ approximation | $\dfrac{\gamma d_e}{k_y \rho_s} \Delta' \ll \rho_s \Delta' \ll 1$ |
| 4 | Neglecting FLR effects in the inner regions | $\rho_e \ll \dfrac{\gamma d_e}{k_y \rho_s}$, |

TABLE 1. Table summarizing the various assumptions.

relation includes a corrective term to (3.8). We derived this dispersion relation using an asymptotic matching method and various assumptions, slightly different from those adopted by Porcelli (1991).

Table 1 gives a review of the assumptions that were adopted on the parameters during our the analysis. The assumption number 1 indicates a slow time variation of the perturbation. The assumption number 2 is the assumption on the scales of the inner region, where electron inertia becomes important and allows the break of the frozen flux condition. The assumption number 3 allows the use of the so-called constant $\psi$ approximation, implying that the dispersion relation is valid for large wavenumbers (Furth *et al.* 1963). The condition 4, imposed to neglect electron FLR, can be verified for a low-$\beta_e$ plasma. From a technical point of view, our new dispersion relation is obtained by solving the equations in the inner layer in real space, unlike in Porcelli (1991) where the corresponding equations are transformed and solved in Fourier space. The result of our linear theory, which is described in more detail in Appendix A, is given by the dispersion relation,

$$\gamma = 2k_y \frac{d_e \rho_s}{\pi \lambda} \Delta' + \frac{\gamma^2 d_e \pi \lambda}{4 k_y \rho_s^2}. \tag{3.9}$$

The first term on the right-hand side of (3.9) is exactly that of the formula (3.8), for $\lambda = 1$. In the parameter regime indicated by table 1, the second term in (3.9) is a small term that provides a correction to the formula (3.8).

A solution of the dispersion relation (3.9), considered in the regime identified by the assumptions of table 1, is

$$\gamma_u = 2k_y \left( \frac{\rho_s^2}{\pi d_e \lambda} - \frac{\rho_s^{3/2} \sqrt{\rho_s - 2d_e^2 \Delta'}}{\pi d_e \lambda} \right), \tag{3.10}$$

and is real for $\rho_s > 2d_e^2 \Delta'$. This new dispersion relation is tested against numerical simulations and compared with the expression (3.8). The numerical solver is pseudospectral and is based on a third-order Adams–Bashforth scheme. The scheme uses numerical filters acting on typical length scales much smaller than the physical scales of the system (Lele 1992). The instability is triggered by perturbing the equilibrium with a disturbance of the parallel electron gyrocentre velocity field. Because of the requirement

https://doi.org/10.1017/S0022377822000010 Published online by Cambridge University Press

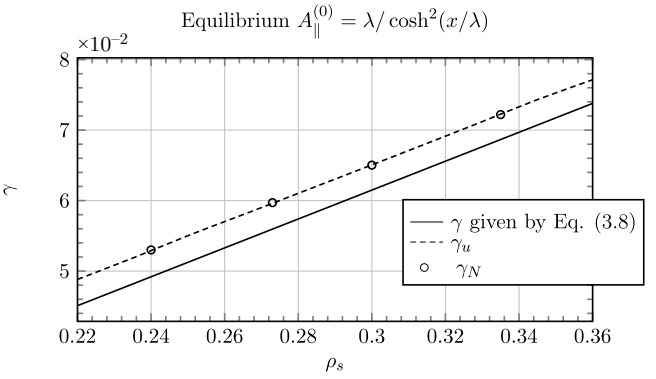



FIGURE 1. Comparison between the analytical growth rate $\gamma_u$ obtained from the new formula (3.10) (dashed line), the analytical growth rate obtained from the formula (3.8) (solid line) and the numerical growth rate $\gamma_N$ defined in (3.12) (circles). The parameters are $d_e = 0.1$, $\lambda = 1$, $\Delta' = 0.72$, $m = 1$. The box size is given by $-10\pi < x < 10\pi$, $-0.48\pi < y < 0.48\pi$. The values of the parameters lie in the regime of validity of the new formula (3.10). One can see that, for different values of $\rho_s$, the correction present in (3.10) yields a better agreement with the numerical values.

of periodic boundary conditions, the equilibrium (3.4*a*,*b*) is approximated by

$$A_\parallel^{(0)}(x) = \sum_{n=-30}^{30} a_n \mathrm{e}^{inx}, \tag{3.11}$$

where $a_n$ are the Fourier coefficients of the function $f(x) = \lambda/\cosh(x/\lambda)^2$ (Grasso *et al.* 2006). The numerical growth rate is determined by the formula

$$\gamma_N = \frac{\mathrm{d}}{\mathrm{d}t} \log \left| A_\parallel^{(1)}\left(\frac{\pi}{2}, 0, t\right)\right|, \tag{3.12}$$

so that $A_\parallel^{(1)}$ is evaluated at the X point, where reconnection takes place.

As shown on figures 1 and 2, the agreement between the theoretical and the numerical values appears to be improved by this new formula, when the latter is applied in its regime of validity. We also performed additional tests on a different equilibrium (the Harris sheet), as shown in figure 2. Also in this case, we observe that our new dispersion relation provides a better agreement with the numerical values. Consequently, (3.10) can be seen as an upgrade of the formula (3.8) in the regime of parameters indicated by table 1.

Figure 3 gives a comparison between the theoretical growth rate predicted by (3.7), (3.8) and (3.10), and the numerical growth rate $\gamma_N$ as a function of the wavenumber $k_y$. According to these tests, $\gamma_u$ seems to give a very good prediction for wavenumbers $k_y > 1.1$. The discrepancy observed for lower values of $k_y$ comes from the fact that the condition allowing the use of the constant $\psi$ approximation, $\Delta' \gamma d_e/(k_y \rho_s) \ll \rho_s \Delta' \ll 1$, is no longer satisfied for a small wavenumber. The breakdown of $\gamma_u$ for $k_y \ll 0.95$ is due to the fact that for $\Delta' > \rho_s/(2d_e^2)$, the solution (3.10) is no longer real.

### 3.2. *Numerical results for $\beta_e \neq 0$*

We now proceed to a numerical study of the model (2.35) and (2.36), complemented by (2.37), (2.38) and (2.39). This will allow us to take into account the effects of finite $\beta_e$.

https://doi.org/10.1017/S0022377822000010 Published online by Cambridge University Press

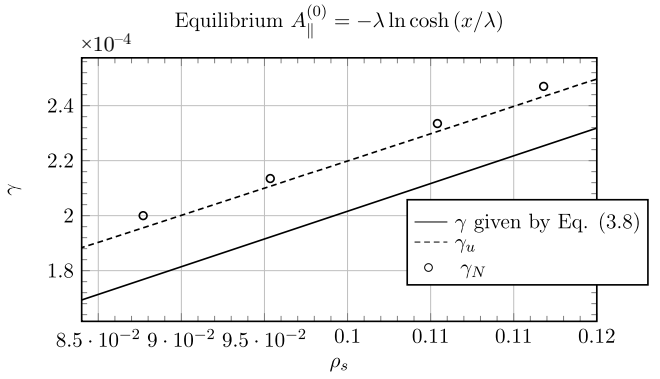



FIGURE 2. This plot is showing additional tests, analogous to those of figure 1, but with the Harris sheet equilibrium $A_{\parallel}^{(0)}(x) = -\lambda \ln\cosh(x/\lambda)$ and $\phi^{(0)}(x) = 0$, for which $\Delta_H^{'} = 2(1/(k_y\lambda) - k_y\lambda)/\lambda$ and using the mode $m = 1$. The parameters are $d_e = 0.2$ and $\lambda = 3$. The box size is $-10\pi < x < 10\pi$, $-4\pi < y < 4\pi$. For this case, $\Delta_H' = 0.38$. For this equilibrium the dispersion relation corresponds to $\gamma_u = k_y(\rho_s^2/(\pi d_e\lambda) - \rho_s^{3/2}(\rho_s - 2d_e^2\Delta_H^{'})^{1/2}/(\pi d_e\lambda))$ and differs from (3.10) by a factor 2 coming from the evaluation of $\mathrm{d}B_{y0}/\mathrm{d}x$ at the X point. Symbols are the same as in figure 1. Also in this case, the new formula yields a better agreement with the numerical values.

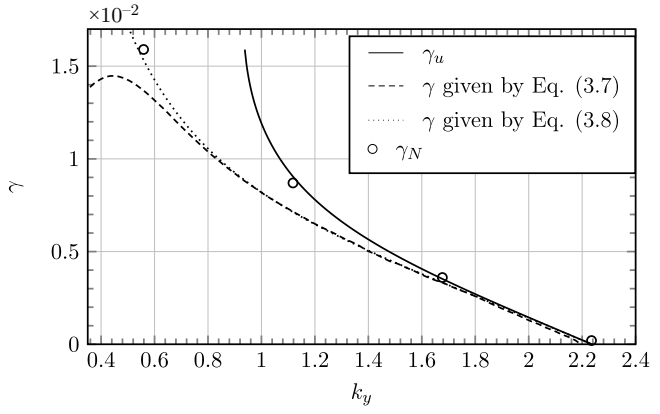



FIGURE 3. Comparison between the theoretical growth rate predicted by (3.7), (3.8) and (3.10), and the numerical growth rate $\gamma_N$ as a function of the wavenumber, $k_y = \pi m/L_y$. The parameters are $d_e = 0.03$, $\rho_s = 0.03$, $\lambda = 1$. The runs were done with the modes $1 \le m \le 4$ and $L_y = 1.789\pi$. The corresponding values of the tearing stability parameter lie in the interval $0.005 \le \Delta' \le 47.86$.

The numerical set-ups are the same as those presented in the previous section, relative to the equilibrium (3.4*a*,*b*), but the code accounts now for finite $\beta_e$ effects. The gyroaverage operators are introduced as they are defined in the Fourier space by (2.14) and (2.15). For the linear tests we focus on a weakly unstable regime for which $0 < \Delta' < 1$. The strongly unstable case shows interesting behaviours in the nonlinear phase and will be studied in the next section. For all the tests, we will use $\lambda = 1$. In order to isolate the contribution coming from purely varying $\beta_e$, we first scan $\beta_e$ from $10^{-3}$ to 1 while $\rho_s$ and $d_e$ remain fixed, which is equivalent to considering a different mass ratio for each $\beta_e$ value. We recall

https://doi.org/10.1017/S0022377822000010 Published online by Cambridge University Press

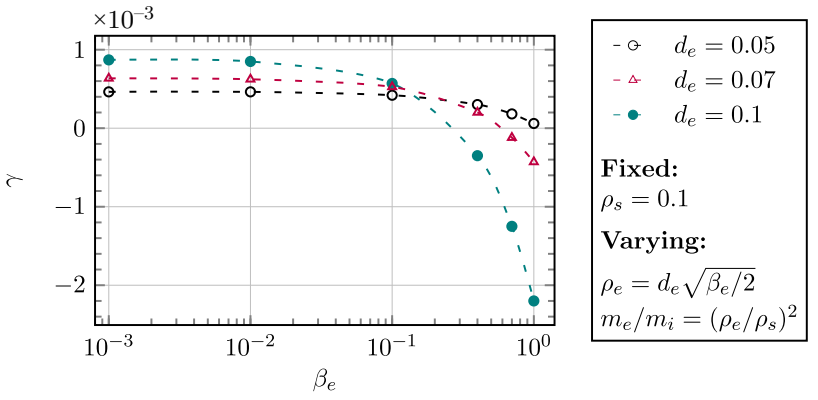



FIGURE 4. Numerical growth rates of the collisionless tearing mode as a function of $\beta_e$, for three different values of $d_e$. The box length along $y$ is such that $-0.45\pi < y < 0.45\pi$, yielding a value of the tearing instability parameter of $\Delta' = 0.067$ for the largest mode in the system. We stand in a very small $\Delta'$ regime, close to a marginal stability when $\beta_e < 0.1$. One sees that for higher values of $\beta_e$, and depending on the value of $d_e$, the mode is stabilized.

that the parameters are indeed linked by the relations

$$\rho_e = \rho_s \sqrt{\frac{m_e}{m_i}} = d_e \sqrt{\frac{\beta_e}{2}}. \tag{3.13}$$

We repeat this scan for three different values of $d_e$. The results are presented in figure 4 and show that the effect of increasing $\beta_e$ and $m_e/m_i$ is stabilizing the tearing mode. This is consistent with the results obtained in the gyrokinetic and collisional study of Numata *et al.* (2011), where $\beta_e$ and the mass ratio are also varied. Figure 4 also shows the competition between the destabilizing effect of the electron inertia and the stabilizing effect of $\beta_e$. For this set of parameters, the influence of $\beta_e$ on the weakly unstable regimes is almost negligible until $\beta_e = 1$. For relatively low values of $\beta_e$, the highest growth rate corresponds to that for which the parameter $d_e$ is the largest. We recall in fact, from § 3.1, that, for $\beta_e \ll 1$, the formulae (3.8) and (3.10) hold. Such formulae, for $d_e \ll 1$, predict that the growth rate increases linearly with $d_e$. Conversely, when $\beta_e$ becomes large enough, as appears for $\beta_e > 0.15$, the growth rate for which $d_e$ is the largest, decreases drastically under the effect of the finite $\rho_e$ and of the parallel magnetic perturbations induced by $\beta_e$.

Some information about the stabilizing role of $\beta_e$ can be inferred by taking the small FLR limit of (2.36), which consists of considering the regime of parameters

$$d_e \ll 1, \quad \rho_s \ll 1, \quad \frac{d_e}{\rho_s} \ll 1, \quad \beta_e = O(1), \tag{3.14a–d}$$

and assuming

$$\nabla_\perp^2 = O(1). \tag{3.15}$$

If we retain the first-order FLR corrections as $d_e, \rho_s \to 0$, the resulting Ohm's law reads

$$\frac{\partial}{\partial t}\left(A_\parallel + \left(\frac{\beta_e}{4} - 1\right) d_e^2 \nabla_\perp^2 A_\parallel\right) + \left[\phi, A_\parallel + \left(\frac{\beta_e}{4} - 1\right) d_e^2 \nabla_\perp^2 A_\parallel\right] + \rho_s^2 \left(\frac{\beta_e}{2+\beta_e} - 1\right) [\nabla_\perp^2 \phi, A_\parallel] = 0. \tag{3.16}$$

https://doi.org/10.1017/S0022377822000010 Published online by Cambridge University Press

The new contributions in (3.16) are those due to finite $\beta_e$ and are not present in the usual two-field model by Schep *et al.* (1994). In particular, the contributions proportional to $(\beta_e/4)d_e^2$ come from electron FLR effects and the contribution proportional to $\beta_e\rho_s^2/(2+\beta_e)$ is due to the presence of the finite $B_\parallel$. In (3.16), comparing with (3.2)–(3.3), it is possible to identify an effective electron skin depth $d_e'$ and an effective sonic Larmor radius $\rho_s'$, given by

$$\frac{d_e'}{d_e} = \sqrt{1 - \frac{\beta_e}{4}} \tag{3.17}$$

and

$$\frac{\rho_s'}{\rho_s} = \sqrt{\frac{2}{\beta_e + 2}}, \tag{3.18}$$

respectively. This argument holds for $d_e'$ purely real and consequently for $\beta_e < 4$. Because $d_e' < d_e$, one can infer that the contribution of $\beta_e$, at the leading order in the expansion (3.14*a–d*)–(3.15), reduces the amplitude of the term that breaks the frozen-in condition. For this reason, one could indeed expect a stabilizing role of $\beta_e$. Deriving rigorously a dispersion relation for tearing modes from the model (2.35)–(2.39), in the general case with finite $\beta_e$, is a very challenging task. In the absence of a rigorous dispersion relation for finite $\beta_e$, a rough but readily available approximation can be obtained from the $\beta_e = 0$ dispersion relation (3.10) (or (3.8)), replacing $d_e$ and $\rho_s$ with the effective parameters $d_e'$ and $\rho_s'$, respectively. This amounts to taking into account the leading-order electron FLR corrections, according to the ordering (3.14*a–d*)–(3.15), in Ohm's law, while neglecting all the $\beta_e$ effects in the electron continuity equation. In particular, higher-order derivative terms (coming from the gyroaverage operators, assuming it is possible to identify the multiplication operator for $k_x$ with $\partial_x$) are neglected, although these can become relevant around the resonant surface and thus influence the growth rate. Using this approximation, it follows immediately that the inclusion of finite $\beta_e$ corrections reduces the growth rate, given that $\gamma \propto d_e'\rho_s'$ (if one considers the leading-order relation given by (3.8)) and that $d_e' < d_e$ and $\rho_s' < \rho_s$. However, the error made with this approximation needs to be checked numerically. We carried out this check by first determining the approximated growth rate in the following way. When replacing $d_e$ and $\rho_s$ by the effective $d_e'$ and $\rho_s'$ in our formula (3.10), valid for small $\Delta'$, we obtain the dispersion relation

$$\gamma_{appr} = \frac{k_y \left( 8\rho_s^2 - (\beta_e + 2)\left(\frac{8\rho_s^2}{\beta_e + 2}\right)^{3/4} \sqrt{\sqrt{\frac{8\rho_s^2}{\beta_e + 2}} + (\beta_e - 4)\Delta' d_e^2} \right)}{\pi\sqrt{4 - \beta_e}(\beta_e + 2) d_e \lambda}. \tag{3.19}$$

We tested the dispersion relation (3.19) against small $\Delta'$ simulations and the results are shown on figure 5. By comparing the analytical formula (3.19) (solid black curve) and the numerical results obtained by the gyrofluid code (black circles), we can see that $\gamma_{appr}$ gives a reasonably good approximation for low $\beta_e$ values, as expected. The red circles in figure 5 show the growth rate obtained using, as input in the fluid code, the effective $d_e'$ and $\rho_s'$, that were calculated on the basis of the values $d_e = 0.1$ and $\rho_s = 0.3$ that we used in the gyrofluid code. The numerical and analytical growth rates obtained from the fluid model replacing $d_e$ and $\rho_s$ with the effective parameters, exhibit a behaviour qualitatively similar to that of the gyrofluid growth rate. However, a significant quantitative difference emerges as $\beta_e$ increases. This is due to the electron FLR contributions that are absent in

https://doi.org/10.1017/S0022377822000010 Published online by Cambridge University Press

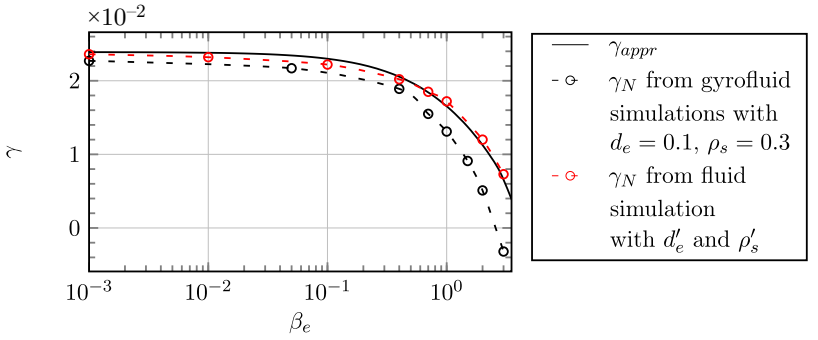



FIGURE 5. Numerical growth rates of the collisionless tearing mode as a function of $\beta_e$. The parameters are $d_e = 0.1$, $\rho_s = 0.3$, $\Delta' = 0.59$, $m = 1$, $k_y = 2.12$, $\lambda = 1$. The solid black curve shows the approximate-$\beta_e$ dispersion relation (3.19). The black circles show the results obtained with the gyrofluid code. The red circles show the results obtained with the fluid code, using, instead of $d_e$ and $\rho_s$, $d'_e$ and $\rho'_s$, given by (3.17)–(3.18).

the approximation. From figure 5 it emerges that the net effect of such contributions is that of further reducing the growth rate, as the curve obtained from the gyrofluid model always lies below those obtained from the effective fluid model.

A further analysis we carried out consists of investigating the effect of $\beta_e$ on the linear growth rate, but at a fixed mass ratio. Physically, this might be interpreted as investigating the effect of the variation of the equilibrium electron temperature $T_{0e}$, supposing that $n_0$, $B_0$, $m_i$, $L$ (and thus the Alfvén frequency, which is the unit of measure of the dimensional growth rate) are fixed. In order to keep a constant mass ratio during the scan in $\beta_e$, we carried out a study with $\beta_e$ ranging from $10^{-3}$ to 2 with $\rho_s$ varying simultaneously. We fix the relation $d_e = \sqrt{m_e/m_i}$ (implying $\rho_s = \sqrt{\beta_e/2}$) and we evaluate the cases $d_e = 0.07$, $d_e = 0.15$, $d_e = 0.1$. Figure 6 shows that when $\beta_e$ and $\rho_s$ are increased simultaneously there seems to be a competition between the destabilizing effect of $\rho_s$ and the stabilizing effect of $\beta_e$. Also in this case, the behaviour at small $\beta_e$, can be interpreted on the basis of the formulae (3.8) and (3.10), predicting an increase of the growth rate with increasing $\rho_s$. When electron FLR effects come into play at larger $\beta_e$, the growth rates decreases. The values chosen for the mass ratio in figure 6 are not realistic. Such values were chosen to show the dependence on the $\beta_e$ parameter more clearly. On the other hand, the mass ratio is not taken as a small parameter in the derivation of the model, so these values are respecting the validity conditions of the model. In the case of the artificial value of $d_e = \sqrt{m_e/m_i} = 0.15$, the stabilizing effect takes over the destabilizing effect of $\rho_s$ even for $\beta_e < 1$. However, for the case $\sqrt{m_e/m_i} = 0.07$, much closer to a real mass ratio, the effect of $\rho_s$ appears to be dominant. Indeed, decreasing $d_e$ at a fixed $\beta_e$ amounts to decreasing $\rho_e$. Thus, for $d_e = 0.07$ the stabilizing effect of the electron FLR terms gets weakened, with respect to the other values of $d_e$, even at large $\beta_e$.

Figure 7 shows the variation of the growth rate of the tearing instability as a function of $\beta_e$, for a fixed value of $\rho_s = 10\rho_e = 0.3$. The obtained results are confirming that the scaling of the growth rate as $\beta_e^{-1/2}$ (or, equivalently, as $d_e$) has been determined with the gyrokinetic study of Numata & Loureiro (2015). This shows the capability of the gyrofluid model to reasonably reproduce gyrokinetic results (Numata *et al.* 2011; Numata & Loureiro 2015) and the fluid theory of Fitzpatrick & Porcelli (2007), in a quantitative way.

https://doi.org/10.1017/S0022377822000010 Published online by Cambridge University Press

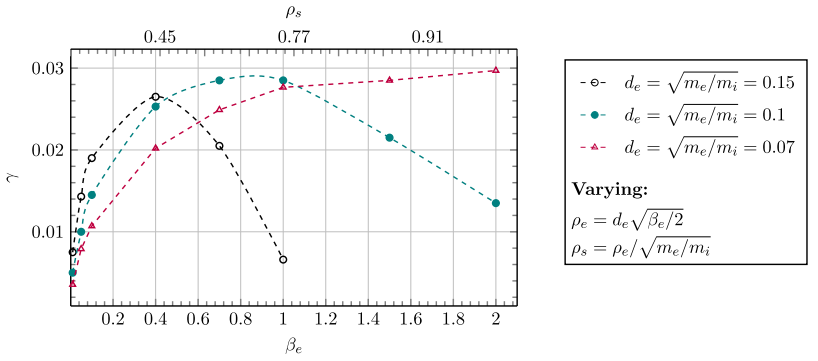



FIGURE 6. Numerical growth rates of the collisionless tearing mode as a function of $\beta_e$ and $\rho_s$, for different values of $d_e = \sqrt{m_e/m_i}$. The box size is $-\pi < x < \pi$, $-0.47\pi < y < 0.47\pi$, which leads to $\Delta' = 0.59$.

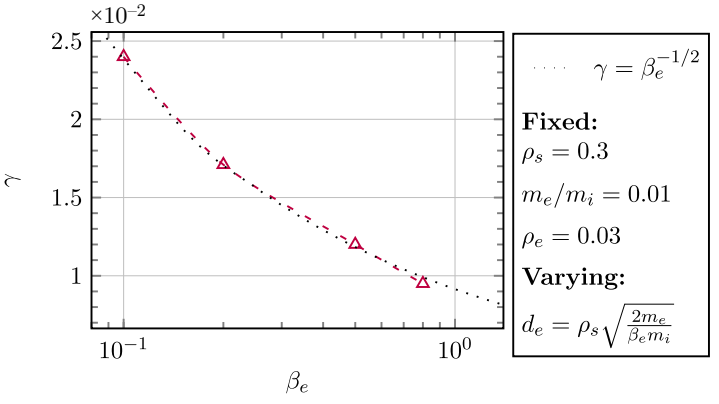



FIGURE 7. The value of $d_e$ for each run increases as $d_e = \rho_s\sqrt{2m_e/(\beta_e m_i)}$. The box size is $-\pi < x < \pi$, $-0.47\pi < y < 0.47\pi$. The numerical values (triangles) are compared with the curve $\gamma = \beta_e^{-1/2}$ (dotted line), which is the scaling predicted by Fitzpatrick & Porcelli (2007) on the basis of a fluid model, and confirmed by gyrokinetic simulations by Numata *et al.* (2011). The comparison shows that also our gyrofluid model confirms such a scaling.

### 3.2.1. *Hot-ion limit, $\tau_i \to +\infty$*

In this article we have focused, so far, on the cold-ion limit, but in this subsection we temporarily deviate from the cold-ion case, to consider the opposite limit, in which $\tau_i = \tau_{\perp i} \to +\infty$. The sole purpose of this subsection is to have a consistent and concise comparison of these two regimes, therefore we will only study the linear behaviour of the hot-ion limit and leave the study of its nonlinear evolution for a future work. The hot-ion limit can actually be of greater interest for space plasmas such as the solar wind. The ion gyrocentre density fluctuation and the ion gyrocentre parallel velocity are still neglected, and therefore the evolution equations remain unchanged. Only the assumption (2.25) is taken in the opposed limit, which has an impact on the development of ion gyroaverage

https://doi.org/10.1017/S0022377822000010 Published online by Cambridge University Press

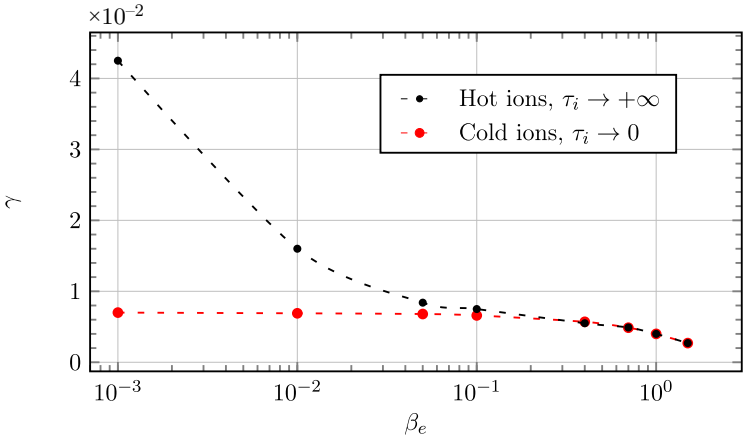



FIGURE 8. Comparison between the linear growth rate obtained in the cold-ion regime and the hot-ion regime. The box size is $-\pi < x < \pi$, $-0.47\pi < y < 0.47\pi$, which leads to $\Delta' = 0.59$.

operators. The static relations (2.37) and (2.39) are thus changed to

$$\phi = \frac{\rho_s^2 N_e}{\left(1 - \dfrac{\beta_e}{2}\right) G_{10e} - G_{10e}^{-1}}, \tag{3.20}$$

$$B_\parallel = \frac{\beta_e}{2\rho_s^2}\phi. \tag{3.21}$$

The linear results obtained in the hot-ion limit are compared with the results obtained in the cold-ion regime on figure 8. The parameters are $d_e = 0.1$, $\rho_s = 0.1$. Our results seem to indicate that, for $\beta_e > 0.5$, the growth rate is very insensitive to the temperature of the ions, which is in agreement with the results obtained by Numata *et al.* (2011). Studies have been carried out with arbitrary ratio between the equilibrium ion and electron temperature in the low-$\beta$ limit, by Porcelli (1991) and Grasso *et al.* (1999), and predict that the growth rate is significantly higher when the temperature of the ion background temperature is higher than that of the electrons. This is indeed what we observe for $\beta_e < 10^{-2}$.

## 4. Nonlinear phase

To study the impact of a finite $\beta_e$ on the nonlinear evolution of the magnetic island, we focus on the strongly unstable case, $\Delta' = 14.31$ ($m = 1$), resulting from a box length along $y$ given by $-\pi < y < \pi$. In this case, the mode $m = 2$ has a positive tearing parameter $\Delta'_2 = 1.23$. The higher harmonics are linearly stable. The box along $x$ is chosen to be $-1.5\pi < x < 1.5\pi$ and allows us to reach a large island without incurring boundary effects. We make use of a resolution up to $2880 \times 2880$ grid points. The mass ratio will be taken as $m_e/m_i = 0.01$ for the following tests.

The first tests are carried out by making a scan in $\beta_e$ from $\beta_e = 0.1$ to $\beta_e = 1.5$ while keeping $d_e = 0.08$ and varying $\rho_s$ as $\rho_s = 0.8\sqrt{\beta_e}/\sqrt{2}$. Increasing $\beta_e$ and $\rho_s$ simultaneously in this way, as stated in § 3.2, amounts to varying the electron background temperature $T_{0e}$. Figure 9 shows the evolution in time of the effective growth rate, given by (3.12), for each simulation. In all these cases, with the exception of $\beta_e = 1.5$, we identify three phases: (1) a linear phase during which the perturbation evolution scales as $\exp(\gamma t)$;

https://doi.org/10.1017/S0022377822000010 Published online by Cambridge University Press

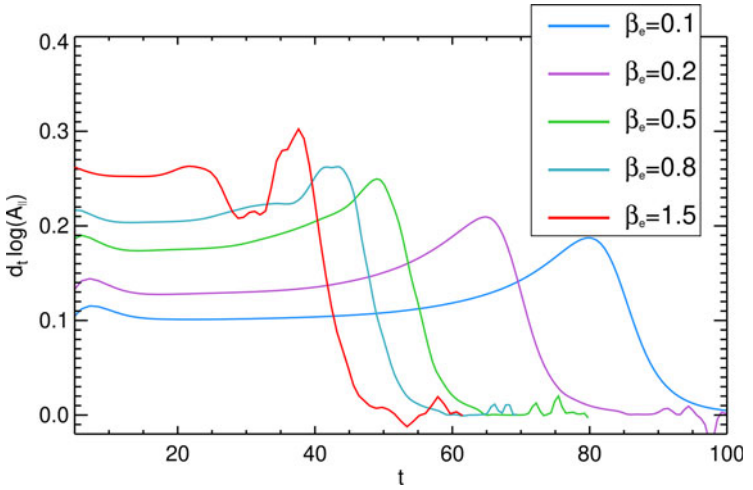



FIGURE 9. Plot of the effective growth rate $(\mathrm{d}/\mathrm{d}t)\log|A_{\parallel}^{(1)}(\pi/2, 0, t)|$, as a function of time. The corresponding values of $\beta_e$ are shown in the table. The value of the electron skin depth is kept fixed to $d_e = 0.08$, whereas $\rho_s$ is varied (and ranges from 0.17 to 0.69) so to keep the mass ratio fixed to $m_e/m_i = 0.01$. All the growth rates, except for the case $\beta_e = 1.5$ exhibit the same behaviour, characterized by a linear, faster than exponential and saturation phase. The case $\beta_e = 1.5$ exhibits also a slowdown phase.

(2) a faster than exponential phase, which is delayed in the case $\beta_e = 0.1$, given that the linear growth rate is smaller, with respect to the case $\beta_e = 0.8$ for which the instability reaches the nonlinear phase faster; (3) a saturation during which the growth rate drops to 0. We point out that, the fact that the linear growth rate increases with increasing $\beta_e$ is related to the fact that $\rho_s$ is also increased for each run. As discussed in the previous section, the isolated effect of an increasing $\beta_e$ in the equations actually implies a stabilization of the linear growth rate. In the case $\beta_e = 0.8$, the nonlinear growth shows a slightly different behaviour from the cases $\beta_e \leq 0.5$ and exhibits a stall phase, during which the growth rate slows down. This stall phase seems to separate two faster than exponential phases. Similar stall phases have been studied in Comisso *et al.* (2013), where a finite ion Larmor radius is considered, and appear to be obtained when considering a large ion Larmor radius. For the case $\beta_e = 1.5$, that we will focus on later, this slowdown is enhanced. We focus now on the case $\beta_e = 0.8$. We scan the values of $d_e$ from 0.06 to 0.1, and $\rho_s = 10\rho_e = 10\sqrt{0.4}d_e \approx 6.32d_e$. The results are shown in figure 10. These curves are compared for a fixed time unit (fixed $v_A$), while keeping $\beta_e$ and the mass ratio constant, which corresponds to varying $B_0 \sim n_0^{1/2}$ while keeping the electron temperature $T_{0e}$ fixed. For the case of $d_e = 0.06$, which corresponds to $\rho_s \sim 0.37$, we observe the slowdown at the end of the linear phase and it is followed by the faster than exponential phase. On the other hand, in the case of $d_e = 0.1$, for which $\rho_s \sim 0.63$, the slowdown appears at a later stage of the evolution process and seems to interrupt the faster than exponential phase by introducing a stall phase. We conclude that the effects of $\beta_e$, and consequently the effects of electron gyrations, causes the appearance of a slowing down phase of the growth of the island during the nonlinear evolution. The larger $\beta_e$, the more distinguishable this slowing phase will be. For a fixed values of $\beta_e$ and $m_e/m_i$, the fact of increasing $d_e$ and $\rho_s$, and consequently increasing the radius of gyration of the electrons, will delay the appearance of this slowing phase.

https://doi.org/10.1017/S0022377822000010 Published online by Cambridge University Press

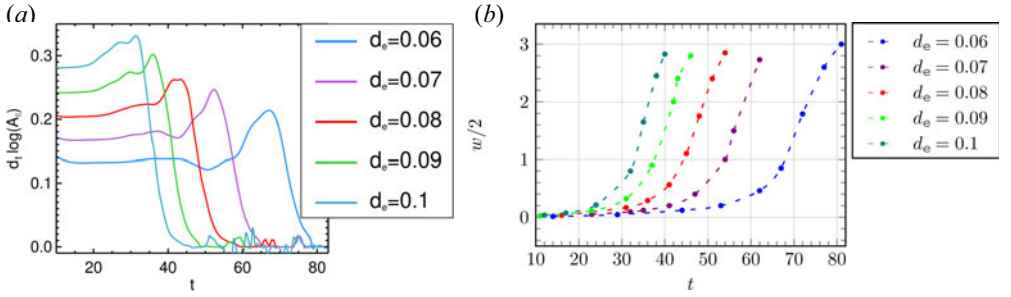



FIGURE 10. (*a*) Plot of the effective growth rate $(\mathrm{d}/\mathrm{d}t)\log|A_{\parallel}^{(1)}(\pi/2, 0, t)|$, as a function of time. The parameters are $\beta_e = 0.8$, implying $\rho_e = \sqrt{0.4}d_e$ and $\rho_s = 10\sqrt{0.4}d_e$. (*b*) Evolution of half-width of the magnetic island until saturation. The simulations correspond to those in panel (*a*).

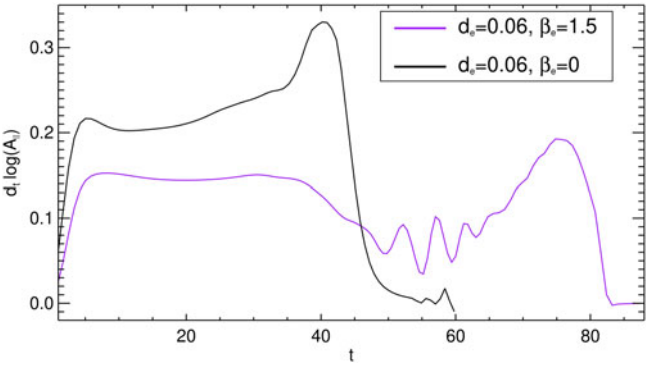



FIGURE 11. Plot of the effective growth rate $(\mathrm{d}/\mathrm{d}t)\log|A_{\parallel}^{(1)}(\pi/2, 0, t)|$, for the cases $\beta_e = 0$ (black curve) and $\beta_e = 1.5$ (purple curve). The other parameters are $\rho_s = 0.519$ and $d_e = 0.06$.

The evolution of the width of the magnetic island for these five runs is shown on the plot on the right-hand side of figure 10. The last point for each run corresponds to the half of the width of the island when the growth rate falls down to zero and enters the saturation phase. In conclusion, the reconnection time simply seems to be longer for smaller $d_e$, but the maximum width before saturation is identical for each case since the amount of initial magnetic energy is the same for each simulation. The last test consists of studying an extreme case for which the slowing down phase is accentuated, which corresponds to the case of $d_e = 0.06$, $\rho_s = 0.519$, $\beta_e = 1.5$. We also perform the simulation for $\beta_e = 0$, using a code that solves the fluid equations (3.2)–(3.3). Figure 11 shows the overplot of the evolution of the growth rate for both simulations as a function of time. The slowing down phase is followed by an oscillation of the nonlinear growth rate. This oscillation was obtained in other tests for which $\beta_e = 1.5$.

In order to understand in detail what causes this slowing down and these oscillations of the island growth that we observe between $t = 43$ and $t = 65$, we compared all the fields for the cases $\beta_e = 0$ and $\beta_e = 1.5$ of figure 11. A remarkable difference between these two regimes concerns the evolution of the inflow and outflow perpendicular velocities, given by $\boldsymbol{U}_\perp = \hat{z} \times \boldsymbol{\nabla}\phi$ and $\boldsymbol{U}_\perp = \hat{z} \times \boldsymbol{\nabla}(G_{10e}\phi - \rho_s^2 2G_{20e}B_\parallel)$, respectively. Figure 12 shows the contour of the components $U_x$ and $U_y$ of the advecting perpendicular velocity for

https://doi.org/10.1017/S0022377822000010 Published online by Cambridge University Press

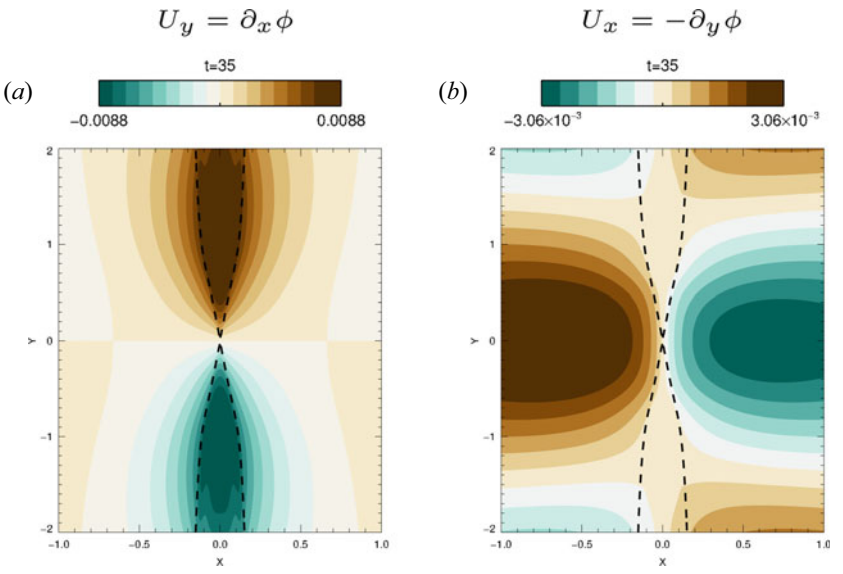



FIGURE 12. Contour plot of the perpendicular velocity component for $\beta_e = 0$ with (*a*) $U_y$ and (*b*) $U_x$. The parameters are the same as those in figure 11. The magnetic island edges are shown by the dotted lines. Not the entire domain is shown.

$\beta_e = 0$. These contours do not show the entire box so that we focus on the island region drawn with the dotted lines. As expected, the contour of $U_y$ shows an outflow leaving the X point and $U_x$ shows an inflow in the direction of the X point.

Figure 13 shows $U_x$ and $U_y$, for $\beta_e = 1.5$, at two different times. For a better comparison we also show the part of the perpendicular velocity only induced by the electrostatic potential $\hat{z} \times \nabla G_{10e}\phi$ on figure 14 to identify the role of $G_{10e}\phi$ and show that its behaviour in the case $\beta_e = 1.5$ is similar to that of the case $\beta_e = 0$. The first time shown in figure 13 corresponds to the beginning of the slowdown of the island growth. We observe that, close to the reconnection region, there is a small region where the velocity changes sign, with respect to the standard $\beta_e = 0$ case. This inversion is more visible for $U_y$, where, inside the island, the fluid velocity is dominated by $B_\parallel$. We can conclude that $G_{10e}\phi \leq \rho_s^2 2G_{20e}B_\parallel$ in the reconnected region. Consequently, the slowing down of the island growth can be explained by the fact that the advection velocity contains an additional drift due to the presence of the magnetic perturbation along the guide field. This effect decelerates the convergence of the field lines towards the reconnection region, where their evolution will be decoupled from that of the fluid. At the time $t = 66$, when the island begins to grow faster than exponentially, the region where $G_{10e}\phi \leq \rho_s^2 2G_{20e}B_\parallel$ shrinks and the advection towards the X point becomes much more effective, allowing the explosive growth.

We now focus on the behaviour of $U_y$ during the small oscillations of the growth rate, visible on figure 11. Figure 15 shows a contour of $U_y$ in the upper part of the domain, between $t = 46$ and $t = 55$. The cell structures indicate two negative peaks. We recall that, in the case of $\beta_e = 0$, we would observe a single positive peak. These peaks are growing at the centre of the island and will follow each other while moving toward the X point. The acceleration or deceleration of the island growth depends on the position (in absolute value) of the highest peak. When the highest peak is closer to the X point, the reconnection

https://doi.org/10.1017/S0022377822000010 Published online by Cambridge University Press

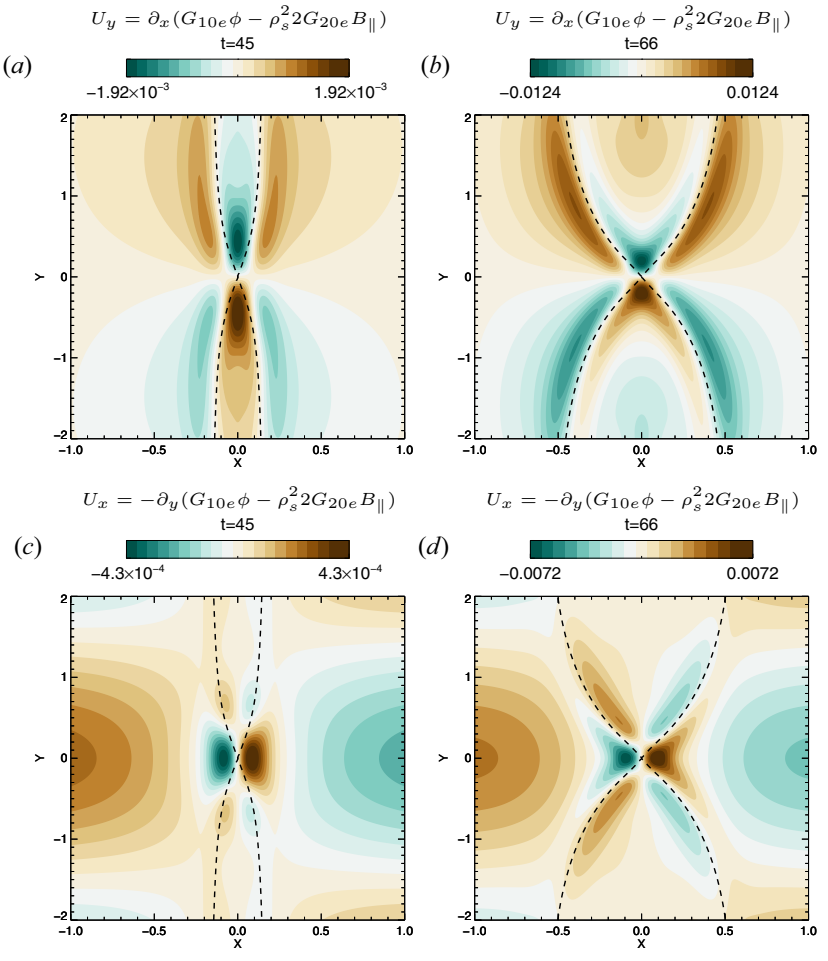



FIGURE 13. Here (*a*,*b*) $U_y$ and (*c*,*d*) $U_x$. For all these contours we used $\beta_e = 1.5$ and the other parameters are the same as those in the figure 11. The magnetic island edges are shown by the dotted lines. Not the entire domain is shown.

rate reaches a maximum ($t = 46$ or $t = 52$). This peak will then decrease while the other one, farther from the X point, will grow ($t = 48$ or $t = 55$). During this part of the cycle, the growth rate reaches a minimum. We interpret this intermittent flow, generated by the presence of $B_\parallel$, as the mechanism responsible for the accelerations and decelerations of the island growth.

### 4.1. *Energy considerations*

The time variations of the different components of the energy for the cases $\beta_e = 0$ and $\beta_e = 1.5$, whose growth rate is shown in figure 11, are shown on figure 16. The variations are defined as $(1/2)\int \mathrm{d}x^2(\xi(x, y, t) - \xi(x, y, 0))/H(0)$ where the function $\xi$ can be replaced by the different contributions of the Hamiltonian (2.31). In terms of the gyrofluid variables and in the presence of FLR effects, identifying the physical meaning of all the contributions to the energy is not obvious. Therefore, we use the terminology adopted in Tassi *et al.* (2018) and which refers to the fluid limit $\beta_e = 0$. The different contributions

https://doi.org/10.1017/S0022377822000010 Published online by Cambridge University Press

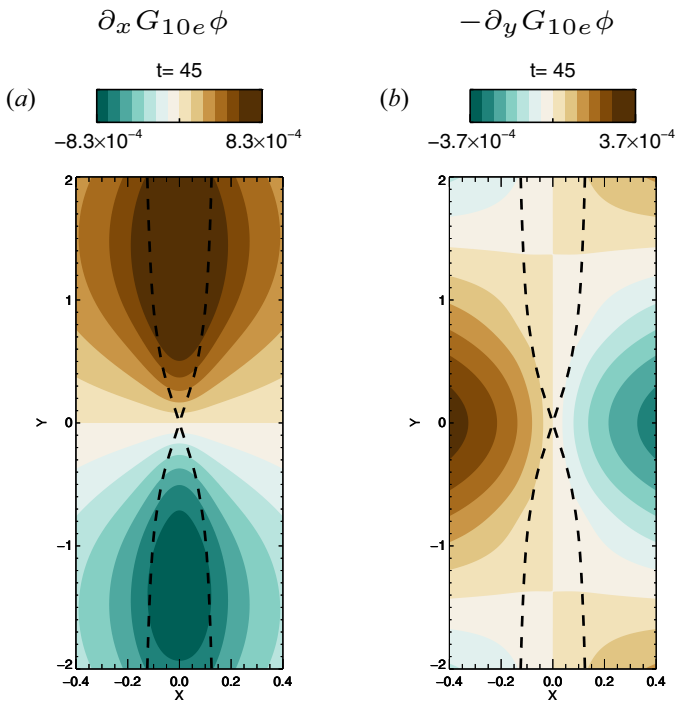



FIGURE 14. Contour plots of the components of the velocity field $\hat{z} \times \nabla G_{10e}\phi$, at t=45. This corresponds to the case $\beta_e = 1.5$ and the other parameters are the same as those in the figure 11. The magnetic island edges are shown by the dotted lines. Not the entire domain is shown.

are: the magnetic energy, $E_{\text{mag}}$, for which $\xi = -U_e G_{10e} A_\parallel$ (reduced to $|\nabla_\perp A_\parallel|^2$ in the fluid case); the parallel electron kinetic energy, $E_{ke}$, for which $\xi = d_e^2 U_e^2$ (reduced to $d_e^2(\nabla_\perp^2 A_\parallel)^2$ in the fluid case); the energy due to the fluctuation of the electron density, $E_{pe}$, for which $\xi = \rho_s^2 N_e^2$ (reduced to $\rho_s^2(\nabla_\perp^2\phi)^2$ in the fluid case); and the perpendicular electrostatic energy of the electrons combined with the energy of the parallel magnetic perturbations, $E_{kp}$, for which $\xi = -(G_{10e}\phi - \rho_s^2 2G_{20e}B_\parallel)N_e$ (reduced to $|\nabla_\perp\phi|^2$ in the fluid case). We consider the simulation as being reliable until the time at which the percentage of the total energy that gets dissipated numerically (black curve) reaches 1 %.

By comparing the two simulations, one can see that there appears to be a comparable amount of magnetic energy being converted. The remarkable difference is the evolution of the component that combines the electrostatic energy and the energy of the parallel magnetic perturbations, $E_{kp}$, which, in the case $\beta_e = 1.5$, also seems to be converted into electron thermal energy ($E_{pe}$), resulting in an increase in this component. This decrease of the electrostatic energy has been observed only in the case $\beta_e = 1.5$. In the case of $\beta_e = 0.8$, it appears that this component stays rather close to its initial value.

We also carried out the test with $\beta_e = 1.5$ by artificially removing the parallel magnetic perturbation $B_\parallel$ from the code, and consequently it was not appearing in the expression of $E_{kp}$. It appeared first that the presence of $B_\parallel$ has a stabilizing effect on the tearing mode (which is consistent with the linear results discussed in § 3.2), and secondly, the energy component $E_{kp}$ was slightly increasing instead of decreasing. This allows us to conclude that the energy related to the parallel magnetic perturbations is in fact the decreasing component that seems to be converted into electron thermal energy $E_{pe}$.

https://doi.org/10.1017/S0022377822000010 Published online by Cambridge University Press

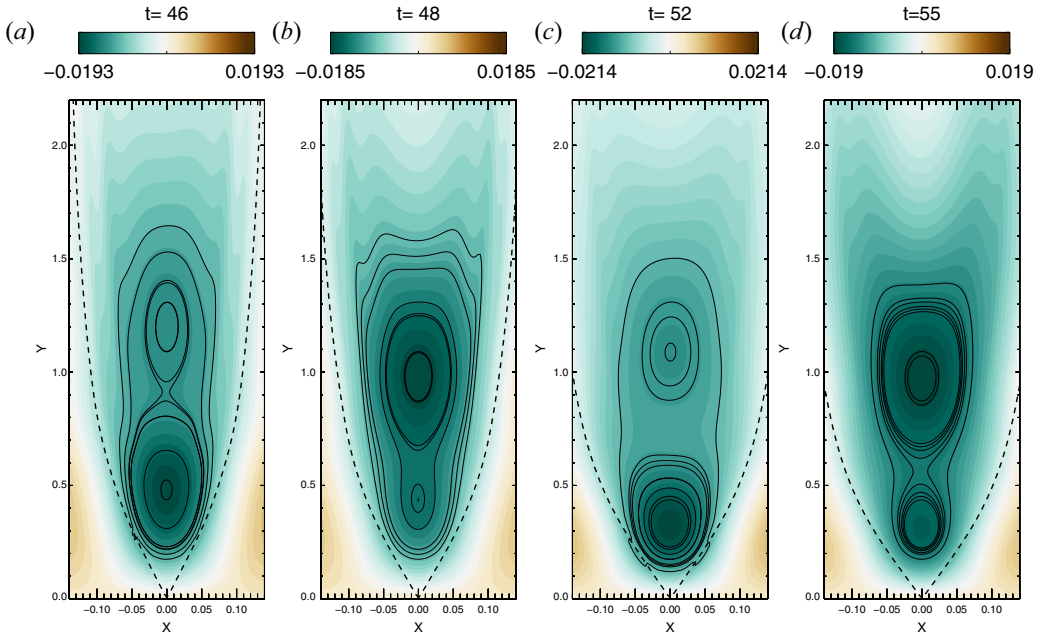



FIGURE 15. Contour plot of $U_y$ showing the upper part of the domain for $\beta_e = 1.5$. The parameters are the same as those in figure 11. The magnetic island edges are shown by the dotted lines. Here $U_y$ is negative inside the island and the cell structures indicate the regions where the flow amplitude is greater. The situations where the highest (in absolute value) peak is closer to the X point ($t = 46$ and $t = 52$) correspond to maxima of the growth rate. Minima of the growth rate occur when the highest peak is far from the X point ($t = 48$ and $t = 55$).

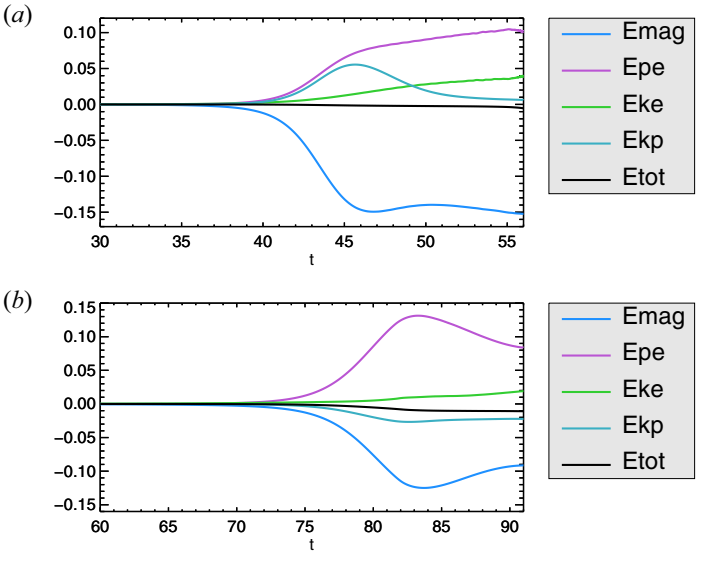



FIGURE 16. Time evolution of the energy variations for the cases $\beta_e = 0$ (*a*) and $\beta_e = 1.5$ (*b*). The parameters are $d_e = 0.06$, $\rho_s = 0.519$ and their corresponding growth rate is shown in figure 11.

https://doi.org/10.1017/S0022377822000010 Published online by Cambridge University Press

**5. Conservation laws of the model**

In this section we discuss the conservation laws of the gyrofluid model and its Lagrangian invariants. Equations (2.35)–(2.36) can be recast in the form

$$\frac{\partial A_\pm}{\partial t} + \boldsymbol{v}_\pm \cdot \nabla A_\pm = 0, \tag{5.1}$$

where

$$A_\pm = G_{10e} A_\parallel - d_e^2 U_e \pm d_e \rho_s N_e, \tag{5.2}$$

$$\boldsymbol{v}_\pm = \hat{z} \times \nabla \left( G_{10e}\phi - \rho_s^2 2 G_{20e} B_\parallel \pm \frac{\rho_s}{d_e} G_{10e} A_\parallel \right). \tag{5.3}$$

We define by

$$\phi_\pm = G_{10e}\phi - \rho_s^2 2 G_{20e} B_\parallel \pm \frac{\rho_s}{d_e} G_{10e} A_\parallel, \tag{5.4}$$

the stream functions of the velocity fields $\boldsymbol{v}_\pm = \hat{z} \times \nabla \phi_\pm$. The formulation (5.1) makes the presence of Lagrangian invariants evident, corresponding to the fields $A_\pm$, in the model. Such Lagrangian invariants are advected by the incompressible velocity fields $\boldsymbol{v}_\pm$. The presence of such Lagrangian invariants is a feature common to many 2-D Hamiltonian reduced gyrofluid models (Waelbroeck, Hazeltine & Morrison 2009; Grasso *et al.* 2010; Waelbroeck & Tassi 2012; Keramidas Charidakos, Waelbroeck & Morrison 2015; Tassi 2017, 2019; Passot, Sulem & Tassi 2018; Grasso & Tassi 2015) and is related to the existence of infinite families of Casimir invariants of the Poisson bracket.

For (2.35)–(2.36), such invariants correspond to the two families

$$C_+ = \int \mathrm{d}^2 x \, \mathcal{C}_+(A_+), \quad C_- = \int \mathrm{d}^2 x \, \mathcal{C}_-(A_-), \tag{5.5a,b}$$

where $\mathcal{C}_\pm$ are arbitrary functions. Equations (5.1) imply that contour lines of the fields $A_\pm$ cannot reconnect, as the corresponding vector fields $\boldsymbol{B}_\pm = \nabla A_\pm \times \hat{z}$ are frozen in the velocity fields $\boldsymbol{v}_\pm$. On the other hand, the same model allows magnetic field lines to reconnect. In particular, it is useful to illustrate the mechanisms breaking the frozen-in condition in this model. This can be done by inspection of (2.36), governing the evolution of $A_\parallel$ and, consequently, of the magnetic field in the plane perpendicular to the guide field, which is given by $\boldsymbol{B}_\perp = \nabla A_\parallel \times \hat{z}$. Equation (2.4) can be rewritten in the following way:

$$\begin{aligned} &\frac{\partial A_\parallel}{\partial t} + \boldsymbol{u} \cdot \nabla A_\parallel \\ &\quad = -\frac{\mathcal{D}}{\mathcal{D}t} \left( \left( \frac{\beta_e}{4} - 1 \right) d_e^2 \nabla_\perp^2 A_\parallel + \sum_{n=2}^{+\infty} \left( \frac{\beta_e}{4n} - (-1)^{n-1} \right) \left( \frac{\beta_e}{4} \right)^{n-1} \frac{(d_e^2 \nabla_\perp^2)^n}{(n-1)!} A_\parallel \right) \\ &\qquad - \rho_s^2 \sum_{n=1}^{+\infty} \frac{1}{n!} \left( \frac{\beta_e}{4} d_e^2 \right)^n [(\nabla_\perp^2)^n A_\parallel, N_e], \end{aligned} \tag{5.6}$$

where

$$\boldsymbol{u} = \hat{z} \times \nabla (G_{10e}\phi - \rho_s^2 2 G_{20e} B_\parallel - \rho_s^2 N_e), \tag{5.7}$$

https://doi.org/10.1017/S0022377822000010 Published online by Cambridge University Press

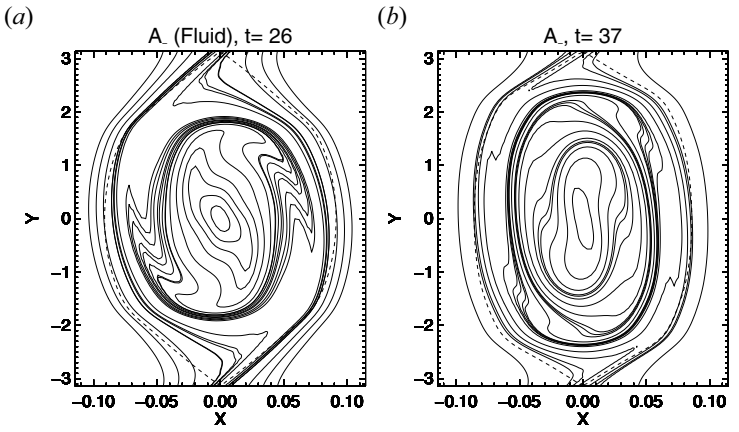



FIGURE 17. Contour plot of the Lagrangian invariant $A_-$ with (*a*) $\beta_e = 0$ and (*b*) $\beta_e = 1.5$. The parameters are $d_e = 0.06$, $\rho_s = 0.519$. The dashed lines are the separatrices. The contour plots refer to the normalized time $\gamma t = 5.18$.

and where the operator $\mathcal{D}/\mathcal{D}t$ is defined by

$$\frac{\mathcal{D}f}{\mathcal{D}t} = \frac{\partial f}{\partial t} + [G_{10e}\phi - \rho_s^2 2G_{20e}B_\parallel, f] \tag{5.8}$$

for a function $f$. In (5.6) we also used the formal expansions

$$G_{10e} = \sum_{n=0}^{+\infty} \frac{1}{n!}\left(\frac{\beta_e}{4}d_e^2\nabla_\perp^2\right)^n, \quad G_{10e}^{-1} = \sum_{n=0}^{+\infty} \frac{(-1)^n}{n!}\left(\frac{\beta_e}{4}d_e^2\nabla_\perp^2\right)^n. \tag{5.9a,b}$$

The right-hand side of (5.6) contains all the terms that break the frozen-in condition. Indeed, if the right-hand side of (5.6) vanishes, the perpendicular magnetic field is frozen in the velocity field $\boldsymbol{u}$. From (5.6) one thus sees that the frozen-in condition can be violated by electron inertia (associated with the parameter $d_e$) and by electron FLR effects (associated with the combination $d_e^2\beta_e/4$). In the limit $\beta_e = 0$ only electron inertia remains to break the frozen-in condition. On the other hand, because electron FLR terms are associated with the product between $\beta_e/4$ and $d_e^2$, in the limit $d_e = 0$ both electron inertia and electron FLR terms disappear and the right-hand side of (5.6) vanishes, thus restoring the frozen-in condition. We remark that the presence of a finite $\beta_e$ is also responsible for finite parallel magnetic perturbations $B_\parallel$. However, these do not violate the frozen-in condition for the perpendicular magnetic field, as they only contribute to modify the advecting velocity field $\boldsymbol{u}$ (the parallel magnetic field lines, on the other hand, might undergo reconnection).

We consider here the qualitative structures of the contour plots of the Lagrangian invariants $A_\pm$ referring to the choice of parameters already adopted for figure 11. From comparing the contour plots of $A_-$, in the case $\beta_e = 0$ (left-hand panel of figure 17) and $\beta_e = 1.5$ (right-hand panel of figure 17), the structures look qualitatively similar. The contour lines of $A_-$ are induced by the velocity fields $\phi_-$ and undergo a phase mixing (the field $A_+$ is winding up identically in the opposite direction, induced by $\phi_+$). The duration of the transient and linear phases are not identical, consequently we compared the fields at the normalized time $\gamma t = 5.18$, which makes it possible to compare the fields when the islands are of comparable size so that they reached the same stage of

https://doi.org/10.1017/S0022377822000010 Published online by Cambridge University Press

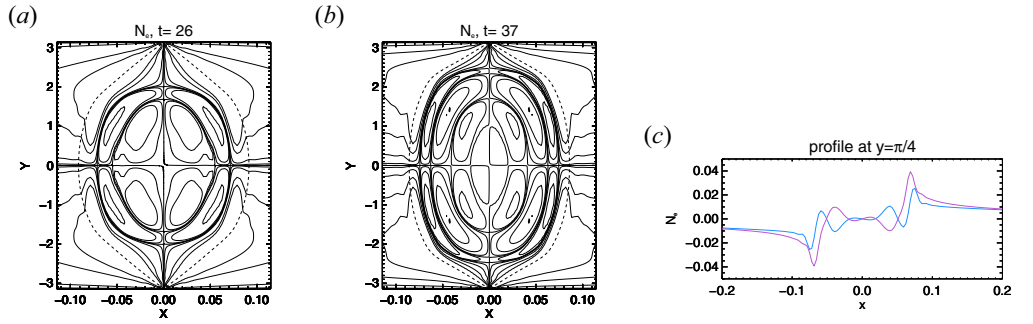



FIGURE 18. Contour plot of the electron density with (*a*) $\beta_e = 0$ and (*b*) $\beta_e = 1.5$. Panel (*c*) are the profiles of $N_e$ at $y = \pi/3$ in the cases $\beta_e = 0$ (purple) and $\beta_e = 1.5$ (blue). The parameters are $d_e = 0.06$, $\rho_s = 0.519$. The dashed lines are the separatrices. The contour plots and profiles refer to the normalized time $\gamma t = 5.18$.

evolution. The separatrices are displayed on each plot by dashed lines. We observe a different shape of the island in the two cases, which reflects the different distribution of the spectral power of the magnetic field. The effect of $\beta_e$ gives a more elongated island along $y$ and thinner along $x$. If we take a $\beta_e > 1$ and keep a low enough mass ratio, then we are forced to stand in a regime with $\rho_s/d_e$ much greater than 1. The ratio considered in this simulation is $\rho_s/d_e = 8.65$. In this case $A_\pm$ is advected by a velocity field which can be approximated by $\boldsymbol{v}_\pm = \pm\hat{z} \times \boldsymbol{\nabla}((\rho_s/d_e)G_{10e}A_\parallel)$, since $\phi_\pm$ tends to coincide with $\pm(\rho_s/d_e)G_{10e}A_\parallel$. Performing other tests (whose results are not shown here) with $d_e \sim \rho_s$, $\beta_e \in \{0, 0.5\}$ and a mass ratio 20 times higher, did not show any obvious difference in the mixing phase either.

The electron density $N_e$ can be obtained by a linear combination of the invariants $A_\pm$:

$$N_e = \frac{A_+ - A_-}{2d_e\rho_s}. \tag{5.10}$$

The contour plot of the electron density is displayed in figure 18 and shows the fine structures produced by the mixing of the Lagrangian invariants $A_\pm$. The case $\beta_e = 1.5$ shows nested quadripolar structures. From the difference between the profiles of $N_e$ in figure 18 it is visible that increasing $\beta_e$ smoothes the gradients in the inner region of the electron density.

## 6. Conclusion

In this article, we have attempted to provide an overview of the impact of finite electron plasma beta effects on the tearing instability in non-collisional plasma with cold ions and a strong guide field. Adopting a gyrofluid model, we have studied the effects of electron gyration and of a parallel magnetic perturbation. There is a wide variety of systems for which this study can be useful, such as magnetosheath plasmas, where current sheets form in the presence of a guide field and a large $\beta_e$ value. Recently, for instance, studies of observations of the magnetospheric multiscale space mission (known as MMS) in the magnetotail have revealed electron-only reconnecting current sheet, where ions do not participate and where $\beta_e$ values can be observed to be greater than 1 (Man *et al.* 2020).

Our main results are the following. First, increasing $\beta_e$ and $\rho_s$ while keeping $d_e$ and the mass ratio fixed, the evolution of the reconnection growth rate seems to be dominated by the destabilizing effect of $\rho_s$, up to a certain threshold where the effects of $\rho_e$ become

https://doi.org/10.1017/S0022377822000010 Published online by Cambridge University Press

important and the growth rate diminishes (figure 6). This can also be interpreted as fixing the background density, $n_0$, the ion mass (so that $d_e$ is fixed) and the guide field amplitude $B_0$, while increasing the electron temperature $T_{0e}$. In the case of a small $\Delta'$ regime, a high $\beta_e$ can eventually stabilize the tearing mode and prevents reconnection from occurring.

Second, in the nonlinear regime of the case $\rho_s \gg d_e$ with $\beta_e \sim m_e/m_i \ll 1$, (which is referred to as being the fluid regime in this article), we retrieved the well known collisionless faster than exponential growth which leads to an explosive growth of the magnetic island. However, when we increase $\beta_e$, this explosive paradigm is modified with the appearance of a slowdown phase preceding the explosive growth. This slowing down is induced by the inclusion of a perpendicular drift that becomes important for finite $\beta_e$ and is due to the presence of a magnetic perturbation along the guide field direction. This drift creates an intermittent velocity opposed to the velocity induced by the electrostatic potential and prevents the convergence of the field lines towards the X point.

A further conclusion is that the effect of $\beta_e$ on the Lagrangian invariants of the gyrofluid model does not seem to reduce the filamentary structure, produced by a 'phase mixing', characteristic of these invariants.

The results obtained with our gyrofluid model are in agreement with results obtained by gyrokinetic studies (Numata *et al.* 2011; Numata & Loureiro 2015). They also complement some two-fluid studies where a consistent accounting for $\beta_e$ effects, including both electron FLR and parallel magnetic perturbations were neglected (Schep *et al.* 1994; Grasso *et al.* 1999; Del Sarto *et al.* 2006; Fitzpatrick & Porcelli 2007).

**Acknowledgements**

The authors acknowledge helpful discussions with D. Laveder.

*Editor T. Passot thanks the referees for their advice in evaluating this article.*

**Funding**

This work benefits from the support of the Ignitor project under the CNR contract DFM.AD003.261 (IGNITOR)-Del. CIPE n.79 del 07/08/2017. The numerical simulations were performed using the EUROfusion high performance computer Marconi Fusion hosted at CINECA (project FUA35-FKMR) and the computing facilities provided by Mesocentre SIGAMME hosted by Observatoire de la Côte d'Azur.

**Declaration of interests**

The authors report no conflict of interest.

**Data availability statement**

The data that support the findings of this study are available from the corresponding author upon reasonable request.

## Appendix A. Calculation of $\gamma_u$

We start from the linearized (3.2)–(3.3), using the equilibrium (3.4*a*,*b*) and the perturbations (3.5*a*,*b*). The perturbations are subject to the boundary conditions $\tilde{A},\ \tilde{\phi} \to 0$, as $x \to \pm\infty$. We look for even solutions of $\tilde{A}(x)$ and odd solutions for $\tilde{\phi}(x)$, which are standard parities for the classical tearing problem.

We consider the time variation of the perturbation being slow,

$$g = \frac{\gamma}{k_y} \ll 1, \tag{A1}$$

https://doi.org/10.1017/S0022377822000010 Published online by Cambridge University Press

and the normalized electron skin depth as a small parameter, i.e.

$$d_e \ll 1. \tag{A2}$$

In order to simplify several expressions in this derivation, we normalize out $\lambda$ by considering the new characteristic length in (2.9*a–c*)–(2.11*a–c*) as given by

$$\bar{L} = \lambda L. \tag{A3}$$

We will reintroduce the original normalization (2.9*a–c*)–(2.11*a–c*) at the end of the derivation, in (A36).

The linearized equations are given by

$$\gamma(\tilde{\phi}'' - k_y^2\tilde{\phi}) - \mathrm{i}k_y A_\parallel B_{y0}'' + \mathrm{i}k_y B_{y0}(\tilde{A}'' - k_y^2\tilde{A}) = 0, \tag{A4}$$

$$\gamma(\tilde{A} - d_e^2(\tilde{A}'' - k_y^2\tilde{A})) + \mathrm{i}k_y\tilde{\phi}(B_{y0} - d_e^2 B_{y0}'') - \mathrm{i}k_y\rho_s^2 B_{y0}(\tilde{\phi}'' - k_y^2\tilde{\phi}) = 0, \tag{A5}$$

where $B_{y0} = -\partial A_\parallel^{(0)}/\partial x$ is the equilibrium magnetic field. In order to solve (A4) and (A5) we have to adopt an asymptotic matching method because the vanishing of the two small parameters $g$ and $d_e$ leads to a boundary layer at the resonant surface $x = 0$. We will consider two spatial regions involving two spatial scales. Far from the resonant surface, located at $x = 0$, the plasma can be assumed to be ideal and electron inertia can be neglected. This region is commonly called the outer region. Close to the resonant surface, we will proceed to a spatial rescaling and get to a scale at which electron inertia becomes important and drives the reconnection process. This second region is called the inner region. We anticipate that we will find a second boundary layer inside the inner region and will need the use of a second asymptotic matching.

**Outer region**

As mentioned before, we assume $d_e \ll 1$ and $g \ll 1$. We then neglect terms of order $d_e^2$ and $g^2$ in (A4) and (A5). The outer equations are given by

$$\tilde{A}_{\mathrm{out}}'' - \left(k_y^2 + \frac{B_{y0}''}{B_{y0}}\right)\tilde{A}_{\mathrm{out}} = 0, \tag{A6}$$

$$\tilde{\phi}_{\mathrm{out}}(x) = \frac{\mathrm{i}g\tilde{A}_{\mathrm{out}}(x)}{B_{y0}}, \tag{A7}$$

where we indicate with the prime symbol the derivative with respect to the argument of the function. The solution for $\tilde{A}_{\mathrm{out}}$ is given by

$$\tilde{A}_{\mathrm{out}}(x) = \exp\left(-|x|\sqrt{k_y^2+4}\right)\left(\frac{15\tanh^3(|x|)}{k_y^2\sqrt{k_y^2+4}} + \frac{15\tanh^2(|x|)}{k_y^2} + \frac{\left(6\left(k_y^2+4\right)-9\right)\tanh(|x|)}{k_y^2\sqrt{k_y^2+4}} + 1\right). \tag{A8}$$

From (A7), on the other hand, one sees that the solution for $\tilde{\phi}_{\mathrm{out}}$ is not defined at the resonant surface $x = 0$, where $B_{y0}$ vanishes. This indicates the presence of the

https://doi.org/10.1017/S0022377822000010 Published online by Cambridge University Press

above-mentioned boundary layer at $x = 0$. We measure the logarithmic derivative of the discontinuity of the outer solutions (A8) at $x = 0$ with the formula (3.6) of the standard tearing parameter, andobtain the expression

$$\Delta' = \frac{2\left(5 - k_y^2\right)\left(k_y^2 + 3\right)}{k_y^2\sqrt{k_y^2 + 4}}. \tag{A9}$$

In the limit $|x| \to 0$ the solution for $\tilde{A}_{\text{out}}$ can be developed using its Taylor expansion

$$\tilde{A}_{\text{out}} = 1 + \frac{\Delta'}{2}|x| + O(x^2). \tag{A10}$$

If $\Delta'$ is small enough, the solution $\tilde{A}$ can be approximated to be equal to 1 in the region where $x \ll 1$. This is standard procedure called the constant $\psi$ approximation (Furth *et al.* 1963).

**Inner region: first boundary layer**

In the inner region, we proceed to a first spatial rescaling using an inner variable, $\hat{x}$, such that

$$x = \epsilon\hat{x}, \tag{A11}$$

where $\epsilon \ll 1$ is a stretching parameter. The rescaling (A11) implies $k_y \ll \partial_{\hat{x}}$, and allows us to use a Taylor expansion of the equilibria (3.4*a*,*b*)

$$B_{y0}(\epsilon\hat{x}) = 2\hat{x}\epsilon + O(\epsilon^2). \tag{A12}$$

We obtain the two inner equations

$$\tilde{A}_{\text{in}}'' = \frac{\mathrm{i}g}{2\epsilon\hat{x}}\tilde{\phi}_{\text{in}}'', \tag{A13}$$

$$g\left(\tilde{A}_{\text{in}} - \frac{d_e^2}{\epsilon^2}\tilde{A}_{\text{in}}''\right) + \mathrm{i}2\epsilon\hat{x}\tilde{\phi}_{\text{in}} - \mathrm{i}\rho_s^2\frac{2\hat{x}}{\epsilon}\tilde{\phi}_{\text{in}}'' = 0. \tag{A14}$$

We introduce the real-valued displacement function

$$\xi_{\text{in}} = -\frac{\mathrm{i}}{g}\tilde{\phi}_{\text{in}}, \tag{A15}$$

and injecting (A13) in (A14), we obtain the layer equation

$$\frac{\xi_{\text{in}}''}{\epsilon^2} - \frac{2\epsilon\hat{x}}{\rho_s^2\left(\dfrac{g^2d_e^2}{\rho_s^2} + 4\epsilon^2\hat{x}^2\right)}\left(2\epsilon\hat{x}\xi_{\text{in}} - 1\right) = 0, \tag{A16}$$

where we used the constant $\psi$ approximation, which, we recall, consists of approximating $\tilde{A}_{\text{in}} \sim 1$ close to $x = 0$. In order to solve (A16) we will assume

$$gd_e \ll \rho_s^2 \ll 1, \tag{A17}$$

and will make use of a second asymptotic matching inside the inner region. We will have indeed two boundary layers at $x = 0$, defining two spatial regions in which the equations

https://doi.org/10.1017/S0022377822000010 Published online by Cambridge University Press

can be solved. A boundary layer exists at the scale $\epsilon_1 = \rho_s$ and a second one at a smaller scale, for $\epsilon_2 = gd_e/\rho_s$.

In the first layer we use

$$\epsilon = \epsilon_1 = \rho_s, \quad \xi_{\text{in}} = \frac{\hat{\xi}}{\epsilon_1}, \tag{A18a,b}$$

where $\hat{\xi}$ is the rescaled displacement function. This choice for $\epsilon$ yields a distinguished limit allowing to retain the maximum number of terms in (A16), as $\epsilon \to 0$, accounting for the condition (A17), which allows us to neglect the term $g^2 d_e^2/\rho_s^2$ in the denominator of (A16). We restrict our study to the case of negligible FLR effects in the inner region, which implies that $\rho_e \ll \epsilon_1$. This condition ensures that the terms responsible for the electron FLR effects remain smaller than those responsible for the effects of electron inertia.

The rescaling leads to the layer equation

$$\hat{\xi}'' - \hat{\xi} = -\frac{1}{2\hat{x}}. \tag{A19}$$

The solution of (A19) is

$$\hat{\xi} = \frac{\mathrm{e}^{\hat{x}}}{4} E_1(\hat{x}) + \frac{\mathrm{e}^{-\hat{x}}}{4}\left(Ei(\hat{x}) - \frac{gd_e}{\rho_s^2}\frac{\pi}{2}\right); \tag{A20}$$

where we already fixed the constants of integration in order to ensure $\lim_{x\to+\infty} \tilde{\xi} = 0$, and to ensure the matching with the solution in the second layer. In (A20) we used the expression of the exponential integral functions

$$E_1(x) = \int_x^{+\infty} \frac{\mathrm{e}^{-t}}{t}\,\mathrm{d}t \quad \text{and} \quad Ei(x) = \int_{-\infty}^{x} \frac{\mathrm{e}^{t}}{t}\,\mathrm{d}t, \quad \text{for } x > 0. \tag{A21a,b}$$

**Inner region: second boundary layer**

In the second layer, where $\hat{x} \sim gd_e/\rho_s^2$, the solution (A20) is no longer valid. Therefore, in the second layer, we perform the following rescaling:

$$\epsilon = \epsilon_2 = \frac{gd_e}{\rho_s}, \quad \xi_{\text{in}} = \frac{gd_e}{\rho_s^3}\bar{\xi}, \tag{A22a,b}$$

and introduce the second inner variable $\bar{x} = x/\epsilon_2$ (so that $\hat{x} = (gd_e/\rho_s^2)\bar{x}$). Since we are at an even smaller spatial scale than that of the previous layer, we also emphasize the condition of neglecting the FLR effects in this second inner layer, i.e. $\rho_e \ll \epsilon_2$.

Considering our assumption (A17), then (A16) becomes

$$\bar{\xi}'' + \frac{2\bar{x}}{(1+4\bar{x}^2)} = 0. \tag{A23}$$

The solution of (A23), written bellow, in terms of the variables $\hat{x}$ and $\hat{\xi}$ reads

$$\hat{\xi}(\hat{x}) = \left(1 - \gamma_E + \frac{gd_e}{2\rho_s^2}\frac{\pi}{2} + \log\left(\frac{\rho_s^2}{gd_e}\right)\right)\hat{x} - \frac{gd_e}{\rho_s^2}\arctan\left(\frac{\rho_s^2\hat{x}}{gd_e}\right) - \frac{1}{4}\log\left(\left(\frac{\rho_s^2\hat{x}}{gd_e}\right)^2 + \frac{1}{4}\right)\hat{x}. \tag{A24}$$

https://doi.org/10.1017/S0022377822000010 Published online by Cambridge University Press

This solution satisfies the boundary condition $\hat{\xi}(0) = 0$, descending from the requirement of $\tilde{\phi}$ being an odd function. In (A24) $\gamma_E$ is the Euler constant.

**$\Delta'$ matching**

We add the following matching condition concerning the derivatives of the solutions:

$$\Delta' = \frac{1}{\epsilon_1} \int_{-\infty}^{\infty} \tilde{A}''_{\text{in}} \, \mathrm{d}\hat{x}. \tag{A25}$$

Using the relations (A13) and (A16) and using the variables $\hat{x}$ and $\hat{\xi}$ we write

$$\Delta' = \frac{2\,g^2}{\rho_s^3} \int_0^{+\infty} \frac{\left(1 - 2\hat{x}\hat{\xi}\right)}{\left(\dfrac{g^2 d_e^2}{\rho_s^4} + 4\hat{x}^2\right)} \, \mathrm{d}\hat{x}. \tag{A26}$$

We separate the integral referring to the second term on the right-hand side of (A26) into two parts, one from 0 to $\sigma$ and one from $\sigma$ to $+\infty$, with $\sigma$ a parameter constrained in the overlap region such that

$$\frac{g d_e}{\rho_s^2} \ll \sigma \ll \frac{1}{\log\left(\dfrac{g d_e}{\rho_s^2}\right)}. \tag{A27}$$

We also recall that $g d_e/\rho_s^2 \ll 1$ is our assumption (A17). Equation (A26) can then be rewritten as

$$\begin{aligned}
\Delta' = {} & \frac{2g^2}{\rho_s^3} \int_0^{+\infty} \frac{1}{\left(\dfrac{g^2 d_e^2}{\rho_s^4} + 4\hat{x}^2\right)} \, \mathrm{d}\hat{x} \\
& - \frac{4g^2}{\rho_s^3} \int_0^{\sigma} \frac{\hat{x}\hat{\xi}}{\left(\dfrac{g^2 d_e^2}{\rho_s^4} + 4\hat{x}^2\right)} \, \mathrm{d}\hat{x} - \frac{4g^2}{\rho_s^3} \int_{\sigma}^{\infty} \frac{\hat{x}\hat{\xi}}{\left(\dfrac{g^2 d_e^2}{\rho_s^4} + 4\hat{x}^2\right)} \, \mathrm{d}\hat{x} \\
= {} & \frac{g\pi}{2 d_e \rho_s} + W_2 + W_1.
\end{aligned} \tag{A28}$$

We calculate the expression (A28) accurate to $g^2/\rho_s^3$ so smaller terms are neglected (the next higher term is of order $(g^2/\rho_s^3)\sigma \log(g d_e/\rho_s^2)$ and thanks to the constraint (A27) we have $\sigma \log(g d_e/\rho_s^2) \ll 1$). In the interval between $\sigma$ and $+\infty$, we use the hypothesis (A17), given by $g d_e \ll \rho_s^2 \ll 1$ to simplify the denominator:

$$\begin{aligned}
W_1 = {} & -\frac{4g^2}{\rho_s^3} \int_{\sigma}^{\infty} \frac{\hat{x}\hat{\xi}}{\left(\dfrac{g^2 d_e^2}{\rho_s^4} + 4\hat{x}^2\right)} \, \mathrm{d}\hat{x} \\
= {} & -\frac{g^2}{\rho_s^3} \int_{\sigma}^{\infty} \frac{\hat{x}}{\left(\dfrac{g^2 d_e^2}{\rho_s^4} + 4\hat{x}^2\right)} \left( \mathrm{e}^{\hat{x}} E_1(\hat{x}) + \mathrm{e}^{-\hat{x}} \left( Ei(\hat{x}) - \frac{g d_e}{\rho_s^2} \frac{\pi}{2} \right) \right) \mathrm{d}\hat{x} \\
= {} & -\frac{g^2}{4\rho_s^3} \int_{\sigma}^{\infty} \frac{1}{\hat{x}} \left( \mathrm{e}^{\hat{x}} E_1(\hat{x}) + \mathrm{e}^{-\hat{x}} Ei(\hat{x}) \right) \mathrm{d}\hat{x} + \frac{g^3 d_e}{4\rho_s^5} \frac{\pi}{2} \int_{\sigma}^{\infty} \frac{\mathrm{e}^{-\hat{x}}}{\hat{x}} \, \mathrm{d}\hat{x}.
\end{aligned} \tag{A29}$$

https://doi.org/10.1017/S0022377822000010 Published online by Cambridge University Press

Using the identity

$$\mathrm{e}^{u}E_1(u) + \mathrm{e}^{-u}Ei(u) = 2\int_0^\infty \frac{u}{u^2+t^2}\sin(t)\,\mathrm{d}t \tag{A30}$$

(from Geller & Ng (1969) (table 3.3)) and knowing that

$$\Gamma(0,\sigma) = \int_\sigma^\infty \frac{\mathrm{e}^{-\hat{x}}}{\hat{x}}\,\mathrm{d}\hat{x} \tag{A31}$$

is the incomplete gamma function whose dominant contribution, as $\sigma \to 0^+$, is $\log(\sigma)$, we obtain

$$W_1 = -\frac{g^2}{4\rho_s^3}\left(\int_0^\infty\int_\sigma^\infty \frac{\sin(t)}{\hat{x}^2+t^2}\,\mathrm{d}\hat{x}\,\mathrm{d}t + O\left(\frac{gd_e}{\rho_s^2}\log(\sigma)\right)\right)\mathrm{d}\hat{x}, \tag{A32}$$

when $\sigma \to 0^+$ and $gd_e/(\rho_s^2\sigma) \to 0^+$. Focusing now on the remaining double integral,

$$\begin{aligned}\int_0^\infty\int_\sigma^\infty \frac{\sin(t)}{\hat{x}^2+t^2}\,\mathrm{d}\hat{x}\,\mathrm{d}t &= \int_0^\infty \sin(t)\frac{\arctan(\hat{x}/t)}{t}\bigg|_\sigma^\infty \mathrm{d}t \\ &= \frac{\pi}{2}\int_0^\infty \frac{\sin(t)}{t}\,\mathrm{d}t - \int_0^\infty \frac{\sin(t)}{t}\arctan(\sigma/t)\,\mathrm{d}t.\end{aligned} \tag{A33}$$

We can prove that the second term is negligible when $\sigma \to 0^+$ by introducing a new small parameter $\kappa$ such as $\sigma \ll \kappa \ll 1$, splitting the integral into the sum of an integral from 0 to $\kappa$ with an integral from $\kappa$ to $+\infty$, and using that in the region $0 < t < \kappa$, $\arctan(\sigma/t) < \pi/2$ and $\sin(t) \sim t$ and in the region $\kappa < t$, one has $\arctan(\sigma/t) \sim (\sigma/t)$. We thus obtain

$$W_1 = -\frac{g^2}{4\rho_s^3}\left(\frac{\pi^2}{2} + O\left(\frac{gd_e}{\rho_s^2}\log(\sigma)\right)\right), \tag{A34}$$

when $\sigma \to 0^+$ and $gd_e/(\rho_s^2\sigma) \to 0^+$.

It is then possible to show, using (A27) and (A17), that

$$W_2 = O\left(\frac{gd_e}{\rho_s^2}\log\left(\frac{gd_e}{\rho_s^2}\right)\right) + O\left(\frac{gd_e}{\rho_s^2}\log(\sigma)\right) + O(\sigma\log(\sigma)) + O\left(\sigma\log\left(\frac{gd_e}{\rho_s^2}\right)\right), \tag{A35}$$

when $\sigma \to 0^+$ and $gd_e/(\rho_s^2\sigma) \to 0^+$.

Summing all the leading-order terms and neglecting the higher-order contributions, we obtain the dispersion relation, written using the normalizing length scale $L$,

$$\Delta' = \frac{g\lambda\pi}{2d_e\rho_s} - \frac{g^2\lambda^2}{4\rho_s^3}\frac{\pi^2}{2}. \tag{A36}$$

It is possible, in view of (A17), to verify that the second term on the right-hand side of (A36) is smaller than the first one ($g/(d_e\rho_s) \gg g^2/\rho_s^3$).

Retaining only the first term in (A36) gives the growth rate predicted by Porcelli (1991) and corresponding to the dispersion relation (3.8). When taking into account the corrective

https://doi.org/10.1017/S0022377822000010 Published online by Cambridge University Press

term, we obtain the expression for the growth rate

$$\gamma_u = 2k_y \left( \frac{\rho_s^2}{\pi d_e \lambda} - \frac{\rho_s^{3/2}\sqrt{\rho_s - 2d_e^2\Delta'}}{\pi d_e \lambda} \right), \tag{A37}$$

corresponding to (3.10). We remark that, because of the parity properties we required on $\tilde{\phi}$ and $\tilde{A}$, the growth rate $\gamma_u$ has to be real, which enforces a further condition of validity, corresponding to

$$\rho_s \geq 2d_e^2\Delta'. \tag{A38}$$

We performed high precision tests to verify the corrective term of the dispersion relation (A37).

## REFERENCES


AYDEMIR, A.Y. 1992 Nonlinear studies of $m = 1$ modes in high-temperature plasmas. *Phys. Fluids* B*: Plasma Phys*. **4** (11), 3469–3472.

BIANCALANI, A. & SCOTT, B.D. 2012 Observation of explosive collisionless reconnection in 3d nonlinear gyrofluid simulations. *Europhys. Lett*. **97** (1), 15005.

BRIZARD, A. 1992 Nonlinear gyrofluid description of turbulent magnetized plasmas. *Phys. Fluids* B*: Plasma Phys*. **4** (5), 1213–1228.

CAFARO, E., GRASSO, D., PEGORARO, F., PORCELLI, F. & SALUZZI, A. 1998 Invariants and geometric structures in nonlinear Hamiltonian magnetic reconnection. *Phys. Rev. Lett*. **80**, 4430–4433.

COMISSO, L., GRASSO, D., TASSI, E. & WAELBROECK, F.L. 2012 Numerical investigation of a compressible gyrofluid model for collisionless magnetic reconnection. *Phys. Plasmas* **19**, 042103.

COMISSO, L., GRASSO, D., WAELBROECK, F.L. & BORGOGNO, D. 2013 Gyro-induced acceleration of magnetic reconnection. *Phys. Plasmas* **20** (9), 092118.

DEL SARTO, D., CALIFANO, F. & PEGORARO, F. 2003 Secondary instabilities and vortex formation in collisionless-fluid magnetic reconnection. *Phys. Rev. Lett*. **91** (23), 235001.

DEL SARTO, D., CALIFANO, F. & PEGORARO, F. 2006 Electron parallel compressibility in the nonlinear development of two-dimensional collisionless magnetohydrodynamic reconnection. *Mod. Phys. Lett.* B **20** (16), 931–961.

DORLAND, W. & HAMMETT, G.W. 1993 Gyrofluid turbulence models with kinetic effects. *Phys. Fluids* B*: Plasma Phys*. **5** (3), 812–835.

EASTWOOD, J.P., MISTRY, R., PHAN, T.D., SCHWARTZ, S.J., ERGUN, R.E., DRAKE, J.F., ØIEROSET, M., STAWARZ, J.E., GOLDMAN, M.V., HAGGERTY, C., *et al.* 2018 Guide field reconnection: exhaust structure and heating. *Geophys. Res. Lett*. **45** (10), 4569–4577.

FITZPATRICK, R. 2010 Magnetic reconnection in weakly collisional highly magnetized electron-ion plasmas. *Phys. Plasmas* **17** (4), 042101.

FITZPATRICK, R. & PORCELLI, F. 2004 Collisionless magnetic reconnection with arbitrary guide field. *Phys. Plasmas* **11** (10), 4713–4718.

FITZPATRICK, R. & PORCELLI, F. 2007 Erratum: collisionless magnetic reconnection with arbitrary guide-field [phys. plasmas 11, 4713 (2004)]. *Phys. Plasmas* **14** (4), 049902.

FURTH, H.P. 1962 Nucl. fusion suppl. *Plasma Phys. Control. Fusion* **1**, 169.

FURTH, H.P. 1964In *Rendiconti della Scuola Internazionale di Fisica Enrico Fermi: Corso XXV : Teoria dei Plasmi*. (ed. M.N. Rosenbluth). Academic Press.

FURTH, H.P., KILLEEN, J. & ROSENBLUTH, M.N. 1963 Finite resistivity instabilities of a sheet pinch. *Phys. Fluids* **6**, 459.

GELLER, M. & NG, E.W. 1969 A table of integrals of exponential integral. *J. Res. Natl Bur. Stand.* B*: Math. Sci*. **73B** (3), 191.

GRASSO, D., CALIFANO, F., PEGORARO, F. & PORCELLI, F. 2001 Phase mixing and saturation in Hamiltonian reconnection. *Phys. Rev. Lett*. **86**, 5051–5054.

GRASSO, D., MARGHERITI, L., PORCELLI, F. & TEBALDI, C. 2006 Magnetic islands and spontaneous generation of zonal flows. *Plasma Phys. Control. Fusion* **48** (9), L87–L95.


https://doi.org/10.1017/S0022377822000010 Published online by Cambridge University Press

GRASSO, D., OTTAVIANI, M. & PORCELLI, F. 2002 Growth and stabilization of drift-tearing modes in weakly collisional plasmas. *Nucl. Fusion* **42** (9), 1067–1074.

GRASSO, D., PEGORARO, F., PORCELLI, F. & CALIFANO, F. 1999 Hamiltonian magnetic reconnection. *Plasma Phys. Control. Fusion* **41** (12), 1497–1515.

GRASSO, D. & TASSI, E. 2015 Hamiltonian magnetic reconnection with parallel electron heat flux dynamics. *J. Plasma Phys*. **81** (5), 495810501.

GRASSO, D., TASSI, E. & WAELBROECK, F.L. 2010 Nonlinear gyrofluid simulations of collisionless reconnection. *Phys. Plasmas* **17** (8), 082312.

KERAMIDAS CHARIDAKOS, I., WAELBROECK, F.L. & MORRISON, P.J. 2015 A Hamiltonian five-field gyrofluid model. *Phys. Plasmas* **22**, 112113.

LELE, S.K. 1992 Compact finite difference schemes with spectral-like resolution. *J. Comput. Phys*. **103** (1), 16–42.

MAN, H., ZHOU, M., YI, Y., ZHONG, Z., TIAN, A., DENG, X.H., KHOTYAINTSEV, Y., RUSSELL, C.T. & GILES, B. 2020 Observations of electron-only magnetic reconnection associated with macroscopic magnetic flux ropes. *Geophys. Res. Lett*. **47** (19), e2020GL089659.

MANDELL, N.R., DORLAND, W. & LANDREMAN, M. 2018 Laguerre–Hermite pseudo-spectral velocity formulation of gyrokinetics. *J. Plasma Phys*. **84** (1), 905840108.

MORRISON, P.J. 1998 Hamiltonian description of the ideal fluid. *Rev. Mod. Phys*. **70**, 467–521.

NUMATA, R., DORLAND, W., HOWES, G., LOUREIRO, N., ROGERS, B. & TATSUNO, T. 2011 Gyrokinetic simulations of the tearing instability. *Phys. Plasmas* **18** (11), 112106.

NUMATA, R. & LOUREIRO, N.F. 2015 Ion and electron heating during magnetic reconnection in weakly collisional plasmas. *J. Plasma Phys*. **81** (2), 305810201.

OTTAVIANI, M. & PORCELLI, F. 1993 Nonlinear collisionless magnetic reconnection. *Phys. Rev. Lett*. **71**, 3802–3805.

PASSOT, T., SULEM, P.L. & TASSI, E. 2018 Gyrofluid modeling and phenomenology of low- $\beta_e$ Alfvén wave turbulence. *Phys. Plasmas* **25** (4), 042107.

PORCELLI, F. 1991 Collisionless $m = 1$ tearing mode. *Phys. Rev. Lett*. **66**, 425–428.

SCHEKOCHIHIN, A.A., COWLEY, S.C., DORLAND, W., HAMMETT, G.W., HOWES, G.G., QUATAERT, E. & TATSUNO, T. 2009 Astrophysical gyrokinetics: kinetic and fluid turbulent cascades in magnetized weakly collisional plasmas. *Astrophys. J. Suppl*. **182** (1), 310–377.

SCHEP, T.J., PEGORARO, F. & KUVSHINOV, B.N. 1994 Generalized two-fluid theory of nonlinear magnetic structures. *Phys. Plasmas* **1**, 2843–2851.

TASSI, E. 2017 Hamiltonian closures in fluid models for plasmas. *Eur. Phys. J.* D **71**, 269.

TASSI, E. 2019 Hamiltonian gyrofluid reductions of gyrokinetic equations. *J. Phys.* A*: Math. Theor*. **52** (46), 465501.

TASSI, E., GRASSO, D., BORGOGNO, D., PASSOT, T. & SULEM, P. 2018 A reduced Landau-gyrofluid model for magnetic reconnection driven by electron inertia. *J. Plasma Phys*. **84** (4), 725840401.

TASSI, E., PASSOT, T. & SULEM, P.L. 2020 A Hamiltonian gyrofluid model based on a quasi-static closure. *J. Plasma Phys*. **86** (4), 835860402.

WAELBROECK, F.L., HAZELTINE, R.D. & MORRISON, P.J. 2009 A Hamiltonian electromagnetic gyrofluid model. *Phys. Plasmas* **16**, 032109.

WAELBROECK, F.L. & TASSI, E. 2012 A compressible Hamiltonian electromagnetic gyrofluid model. *Commun. Nonlinear Sci. Numer. Simul*. **17**, 2171.

https://doi.org/10.1017/S0022377822000010 Published online by Cambridge University Press